

# EROAM: Event-based Camera Rotational Odometry and Mapping in Real-time

Wanli Xing<sup>1,2</sup>, Shijie Lin<sup>1,2</sup>, Linhan Yang<sup>1,2</sup>, Zeqing Zhang<sup>1,2</sup>, Yanjun Du<sup>3</sup>,  
Maolin Lei<sup>4</sup>, Yipeng Pan<sup>1,2</sup>, Chen Wang<sup>1,2</sup>, and Jia Pan<sup>1,2†</sup>

**Abstract**—This paper presents EROAM, a novel event-based rotational odometry and mapping system that achieves real-time, accurate camera rotation estimation. Unlike existing approaches that rely on event generation models or contrast maximization, EROAM employs a spherical event representation by projecting events onto a unit sphere and introduces Event Spherical Iterative Closest Point (ES-ICP), a novel geometric optimization framework designed specifically for event camera data. The spherical representation simplifies rotational motion formulation while operating in a continuous spherical domain, enabling enhanced spatial resolution. Our system features an efficient map management approach using incremental k-d tree structures and intelligent regional density control, ensuring optimal computational performance during long-term operation. Combined with parallel point-to-line optimization, EROAM achieves efficient computation without compromising accuracy. Extensive experiments on both synthetic and real-world datasets show that EROAM significantly outperforms state-of-the-art methods in terms of accuracy, robustness, and computational efficiency. Our method maintains consistent performance under challenging conditions, including high angular velocities and extended sequences, where other methods often fail or show significant drift. Additionally, EROAM produces high-quality panoramic reconstructions with preserved fine structural details.

**Index Terms**—Event-based Vision, Simultaneous localization and mapping (SLAM).

VIDEO, SOURCE CODE AND DATA

Project page: <https://wlxing1901.github.io/eroam/>

## I. INTRODUCTION

**R**OTATIONAL motion estimation represents a fundamental challenge in computer vision and robotics, serving as a cornerstone for various applications from visual odometry to camera stabilization and panoramic image creation [1]. While traditional frame-based cameras have been widely used for this task, they struggle with rapid rotations due to inherent limitations such as motion blur, limited exposure control, and large inter-frame displacements that compromise data association and motion estimation accuracy.

This research is supported by the Jiangsu-Hong Kong-Macau Project BZ2024061, RGC grants (GRF 17201025, GRF 17200924, NSFC-RGC Joint Research Scheme N\_HKU705/24, CRF C1073-24GF), and the Natural Science Foundation of China (Project Number 62461160309).

<sup>1</sup>Department of Computer Science, The University of Hong Kong, Hong Kong SAR, China. e-mail: wlxing@connect.hku.hk

<sup>2</sup>Centre for Transformative Garment Production, Hong Kong SAR, China.

<sup>3</sup>Department of Mechanical and Automation Engineering, The Chinese University of Hong Kong, Hong Kong SAR, China.

<sup>4</sup>Humanoids and Human Centered Mechatronics Research Line, Istituto Italiano Di Tecnologia (IIT), Genoa, Italy.

<sup>†</sup>Corresponding author.

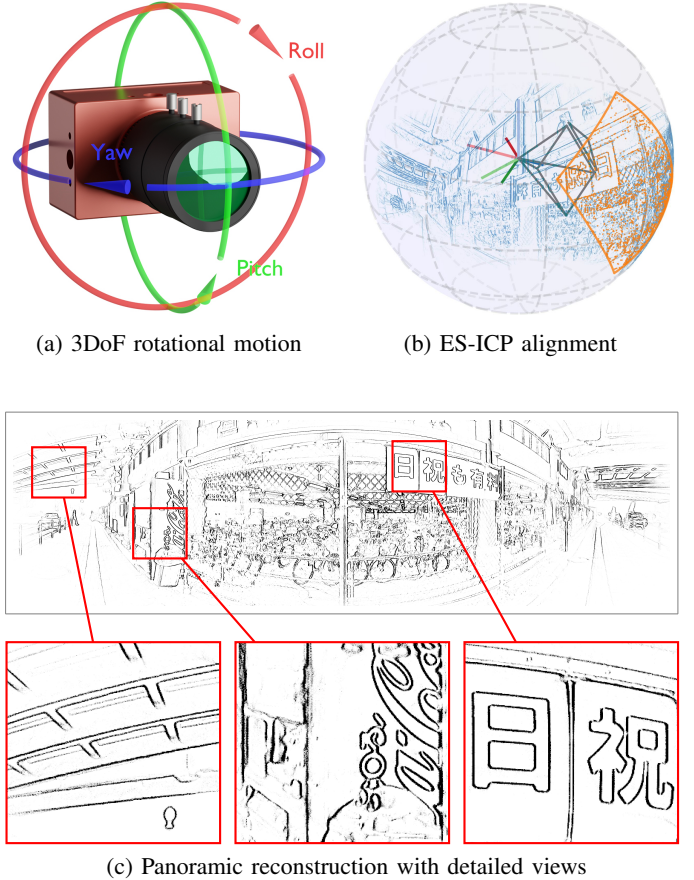


Fig. 1: Event-based 3DoF camera pose estimation and panoramic reconstruction. (a) Our method accurately estimates the 3DoF pose of an event camera from continuous event streams. (b) Events are projected onto a unit sphere and aligned using our novel Event Spherical Iterative Closest Point (ES-ICP) algorithm. (c) The aligned event sphere enables the reconstruction of a clear panoramic image with preserved fine details.

Event cameras [2]–[4] offer a promising alternative through their bio-inspired design. Unlike conventional cameras that capture intensity frames at fixed intervals, these sensors operate asynchronously, measuring and reporting per-pixel brightness changes with microsecond precision. Each event is encoded as a tuple  $e_k = (\mathbf{x}_k, t_k, p_k)$ , where  $\mathbf{x}_k = (u_k, v_k)^T$  denotes the pixel location,  $t_k$  the timestamp, and  $p_k$  the polarity of the brightness change [5]. This unique operating principle enables exceptional temporal resolution, high dynamic range (up to 140 dB), and low power consumption (20 mW) [4],

making event cameras particularly well-suited for challenging scenarios involving high-speed motion or extreme lighting conditions.

The advantages of event cameras have been demonstrated across numerous applications, including SLAM and odometry [6]–[12], robotic navigation [13]–[16], feature extraction and tracking [17]–[21], optical flow estimation [22]–[25], video enhancement [26]–[28], 3D reconstruction [29]–[32], and optical systems [33]–[36]. Recent manufacturing advances have further accelerated their adoption by enabling higher-resolution sensors at more accessible price points [37].

In the specific context of rotational motion estimation, event cameras offer unique advantages through their high temporal resolution and freedom from motion blur, enabling potential accurate capture of rapid rotational movements that conventional cameras struggle to handle. Existing event-based approaches broadly fall into two categories. Event Generation Model (EGM) based methods [38], [39] explicitly model the event triggering process, requiring careful consideration of the contrast threshold and event generation mechanisms. In contrast, Contrast Maximization (CM) based approaches [5], [40], [41] estimate angular velocity by optimizing the alignment of events over temporal windows. While both approaches have demonstrated promising performance in scenarios with moderate and short-term rotational motion, they face significant challenges in more complex scenarios: EGM methods struggle with the complexity of accurately modeling event generation, while CM techniques may lack robustness during highly dynamic rotations involving rapid direction changes. Moreover, both approaches operate on discretized representations with predefined resolutions, introducing inherent quantization errors. Beyond these algorithmic limitations, both approaches often incur substantial computational overhead, limiting their real-time applicability. Additionally, these methods typically lack efficient mechanisms for incremental map updates during long-term operation, leading to increasing computational burden and memory consumption as the observed scene expands.

Drawing inspiration from successful techniques in LiDAR SLAM [42]–[46], we propose a novel approach that addresses these limitations. As illustrated in Fig. 1, our method introduces three key innovations: a spherical event representation, the Event Spherical Iterative Closest Point (ES-ICP) algorithm, and an efficient incremental map management approach. The spherical representation projects events onto a unit sphere, assigning continuous  $\mathbb{R}^3$  coordinates instead of working with discrete pixel locations. ES-ICP is a novel geometric optimization framework specifically designed for event data, which efficiently aligns sparse event point clouds on the unit sphere through parallel point-to-line optimization. Unlike existing methods that operate on discretized maps with fixed resolutions, our approach maintains both tracking and mapping in continuous spherical space, completely decoupling the core estimation pipeline from any discretization requirements. This continuous representation, combined with the innovative ES-ICP algorithm, not only enables precise motion estimation but also allows for flexible panoramic image generation at arbitrary resolutions as a post-processing step. Our incremental map management strategy utilizing dynamic k-d tree structures

and regional density control ensures optimal computational performance even during extended operation. The result is a real-time capable system that provides accurate and robust event camera rotation estimation.

Our main contributions are:

- 1) We introduce a novel spherical event representation that operates entirely in continuous  $\mathbb{R}^3$  space, with efficient incremental map management, enabling accurate motion estimation while decoupling the tracking process from panorama generation, which allows for flexible panoramic image creation at arbitrary resolutions;
- 2) We develop the Event Spherical Iterative Closest Point (ES-ICP) algorithm, which efficiently matches and aligns event projections in continuous spherical space for robust rotational motion estimation;
- 3) We conduct comprehensive experimental validation on both synthetic and real-world datasets, demonstrating superior accuracy and robustness across diverse scenarios, and release our complete implementation and datasets to benefit the research community.

## II. RELATED WORKS

Event-based rotational motion estimation presents unique challenges and opportunities due to the asynchronous nature of event cameras. As summarized in Tab. I, existing approaches have evolved along two main paradigms: Event Generation Model (EGM) based methods, which explicitly model the event triggering process, and Contrast Maximization (CM) based methods, which focus on event alignment optimization. This section analyzes the fundamental principles, practical implementations, and inherent limitations of each approach, providing insights into their relative strengths and weaknesses.

### A. Event Generation Model Based Methods

EGM-based approaches model event triggering conditions. An event triggers when log intensity change exceeds the threshold  $C$ :

$$\Delta L(\mathbf{x}_k, t_k) = L(\mathbf{x}_k, t_k) - L(\mathbf{x}_k, t_k - \Delta t_k) = p_k C \quad (1)$$

where  $\mathbf{x}_k = (u_k, v_k)^\top$  represents the pixel coordinates,  $L(\mathbf{x}_k, t_k)$  is the log intensity at pixel  $\mathbf{x}_k$  at time  $t_k$ ,  $\Delta t_k$  is the time elapsed since the last event at the same pixel,  $p_k \in \{+1, -1\}$  is the polarity of the event, and  $C > 0$  is the contrast threshold [2], [4].

In practice, real event cameras exhibit more complex behavior due to sensor noise, transistor mismatch, and varying illumination conditions. This probabilistic nature is often modeled using normal distributions centered at the contrast threshold  $C$  [2], [47], [48]. For small time intervals  $\Delta t_k$ , the relationship between events and temporal brightness changes can be approximated as:

$$\frac{\partial L}{\partial t}(\mathbf{x}_k, t_k) \approx \frac{p_k C}{\Delta t_k} \quad (2)$$

This approximation serves as the foundation for various event-based algorithms [49]–[52].

TABLE I: Comparison of Event-based Rotational Motion Estimation Methods

Method	Principle	Real-time	GPU Required	Representation	Threshold $C$ Dependency	Polarity Dependency
SMT [38]	EGM	No	No	Discrete	Yes	Yes
RTPT [39]	EGM	No	Yes	Discrete	No	No
CM-GAE [41]	Contrast Maximization	No	No	Discrete	No	Yes
CMax-SLAM [40]	Contrast Maximization	No	No	Discrete	No	No
EROAM (ours)	ES-ICP	Yes	No	Continuous Spherical	No	No

1) *Simultaneous Mosaicing and Tracking (SMT)*: SMT [38] introduced the first comprehensive approach to event-based visual processing by simultaneously addressing camera tracking and scene reconstruction. The method employs a dual-filter architecture: a particle filter for camera rotation tracking and pixel-wise Extended Kalman Filters (EKFs) for mapping. In the tracking module, camera poses are estimated by evaluating how well each pose hypothesis aligns with the current gradient map using an event likelihood model. Concurrently, the mapping module maintains and updates a gradient map through EKF filtering of incoming events, with each pixel independently tracking its gradient estimate and uncertainty.

The key innovation of SMT lies in its probabilistic treatment of both tracking and mapping components, which work symbiotically: the tracker leverages the gradient map for pose evaluation, while the mapping system utilizes pose estimates for gradient updates. This approach effectively handles the asynchronous nature of event data while maintaining a coherent scene representation.

2) *Real-Time Panoramic Tracking (RTPT)*: RTPT [39] advances event-based motion estimation through a direct optimization approach. The method introduces a probabilistic map that tracks event occurrence likelihoods at each spatial location, dynamically updating as the camera moves. Camera pose estimation is formulated as an energy minimization problem that elegantly combines re-projection error with temporal motion smoothness.

A significant contribution of RTPT is its probabilistic map representation, which maintains both observed event counts and possible event occurrences for each location. This formulation naturally accommodates the sparse and asynchronous characteristics of event data while preserving scene geometry in map updates. However, achieving real-time performance requires GPU acceleration, and the method faces challenges with map updates at higher resolutions.

**Limitations of EGM Based Methods.** EGM-based approaches face several fundamental challenges:

- Both SMT and RTPT struggle with robustness to sensor noise and varying illumination conditions, despite their different approaches to handling contrast threshold specification.
- The computational requirements for map updates become prohibitive at higher resolutions, even with GPU acceleration.
- The use of discretized map storage inherently introduces quantization errors that affect motion estimation accuracy.

## B. Contrast Maximization Based Methods

The contrast maximization framework, introduced by Gallego and Scaramuzza [5], [53], represents a fundamentally different approach to event-based motion estimation. The key insight is that when events are warped (rotated) according to the true motion parameters, they align to create sharp edge patterns.

The framework formulates motion estimation as an optimization problem:

$$\omega^* = \operatorname{argmax}_{\omega} \operatorname{Var}(I(\omega, \mathcal{E})) \quad (3)$$

where  $\omega$  is the angular velocity vector to be estimated, and  $I(\omega, \mathcal{E})$  represents an image formed by warped events. This image is created by:

$$I(\mathbf{x}; \omega) = \sum_k \pm_k \delta(\mathbf{x} - \mathbf{x}'_k(\omega)) \quad (4)$$

where  $\pm_k$  is the polarity of each event, and  $\mathbf{x}'_k(\omega)$  represents the warped (rotated) position of the original event according to the candidate angular velocity  $\omega$ . The Dirac delta function  $\delta$  accumulates event polarities at the warped locations.

The quality of motion estimation is measured through the image variance:

$$\operatorname{Var}(I(\omega, \mathcal{E})) = \frac{1}{|\Omega|} \int_{\Omega} (I(\omega, \mathcal{E})(\mathbf{x}) - \mu(I(\omega, \mathcal{E})))^2 d\mathbf{x} \quad (5)$$

where  $\Omega$  is the image domain. The variance measures the contrast of the warped event image - when events are correctly aligned according to the true motion, they form sharp edges resulting in maximum contrast.

1) *Global Events Alignment for Rotational Motion Estimation (CM-GAE)*: CM-GAE [41] enhances the contrast maximization framework through a dual-optimization strategy aimed at reducing drift. The method maintains a global event image by continuously aligning observed events to the initial camera coordinate frame, enabling both local and global consistency checks. Beyond maximizing contrast within temporal windows, CM-GAE introduces a second optimization step that aligns locally warped event images with the accumulated global event image, effectively reducing the drift accumulation common in local optimization methods.

2) *Event-based Rotational SLAM System (CMax-SLAM)*: CMax-SLAM [40] represents a significant advancement as the first complete event-based rotational SLAM system incorporating both front-end and back-end components. The front-end employs contrast maximization for angular velocity estimation, while the back-end performs continuous-time trajectory refinement using B-splines. A key innovation lies in its formulation of bundle adjustment based on contrast

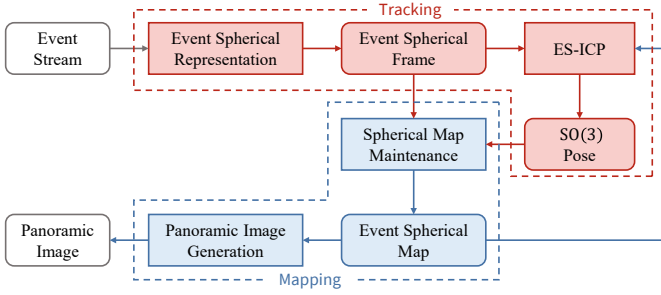


Fig. 2: System Overview: The proposed event-based rotational motion estimation system consists of two main modules. The **tracking module** processes event streams to estimate  $SO(3)$  pose using spherical representation and ES-ICP. The **mapping module** maintains and updates the spherical event map, which supports both tracking and panoramic image generation.

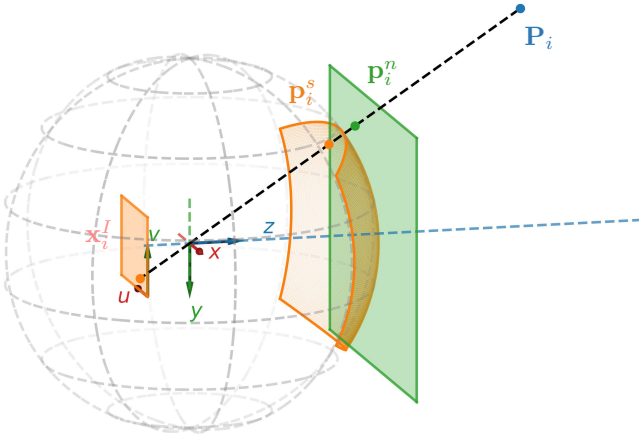


Fig. 3: Spherical projection process: The 3D point  $P_i$  is first projected onto the image plane as  $x_i^I$ . After undistortion and normalization, it becomes  $p_i^s$  on the normalized image plane. Finally,  $p_i^s$  is projected onto the unit sphere, resulting in the spherical point  $p_i^s$ .

maximization, optimizing camera trajectories while simultaneously generating sharp panoramic maps as a by-product of the optimization process.

**Limitations of CM Based Methods.** Contrast maximization approaches face several key challenges:

- The temporal window selection presents an inherent trade-off between having sufficient events for optimization and maintaining the constant angular velocity assumption.
- Iterative optimization and repeated event warping operations impose significant computational overhead.
- The optimization process can encounter local optima [54] and degenerate solutions affecting estimation reliability.
- Global optimization approaches introduce substantial computational demands that impact real-time performance.

### III. METHODOLOGY

#### A. System Overview

Our proposed event-based rotational motion estimation system, illustrated in Fig. 2, comprises two main components: a tracking module and a mapping module. The system is

TABLE II: Summary of Key Symbols and Variables

Symbol	Description
$e_i$	Individual event $(u_i, v_i, t_i, p_i)$
$x_i^I$	Pixel coordinates $(u_i, v_i)^T$
$\mathbf{K}$	Camera intrinsic matrix
$\mathbf{f}(\cdot)$	Distortion function
$\mathbf{f}^{-1}(\cdot)$	Undistortion function
$x_i^u$	Undistorted pixel coordinates
$\mathbf{p}_i^n$	Normalized coordinates on virtual imaging plane
$\mathbf{p}_i^s$	Spherical representation of an event
$\mathbf{p}_i^c$	Cylindrical projection of a point
$\mathcal{E}^s$	Event spherical frame
$f$	Event spherical frame formation frequency
$n$	Number of events per spherical frame
$\mathbf{R}$	Rotation matrix in $SO(3)$
$\mathbf{t}$	Translation vector
$\omega$	Angular velocity of the event camera
$\mathcal{M}^s$	Spherical event map
$\theta_i$	Rotation threshold for key frames
$\mathbf{d}$	Direction vector of fitted line (ES-ICP)
$\mathbf{c}$	Point on fitted line (ES-ICP)
$\mathbf{J}_i$	Jacobian matrix for each point (ES-ICP)
$\mathbf{H}$	Approximated Hessian matrix (ES-ICP)
$\Delta\mathbf{x}$	Incremental update in $so(3)$ (ES-ICP)
$\mathbf{g}$	Gradient vector (ES-ICP)
$\phi_v$	Vertical field of view (panoramic)
$\phi_h$	Horizontal span angle (panoramic)
$\exp(\cdot)^\wedge$	Exponential map from $so(3)$ to $SO(3)$
$\log(\cdot)^\vee$	Logarithm map from $SO(3)$ to $so(3)$
$(\cdot)^\wedge$	Hat operator (vector to skew-symmetric matrix)
$(\cdot)^\vee$	Vee operator (skew-symmetric matrix to vector)
$\ \cdot\ _2$	Euclidean (L2) norm

designed for real-time operation at high frequencies (1000 Hz) with stable computational costs throughout extended operation.

The tracking module begins by transforming incoming events into a spherical representation (III-B). These spherical events are then grouped into event frames and undergo motion compensation (III-C). The compensated event frames serve as input for our novel Event Spherical Iterative Closest Point (ES-ICP) algorithm (III-D). High-frequency operation is crucial for ES-ICP's success, as it ensures that consecutive frames have minimal rotation differences, providing excellent initial guesses that help the algorithm avoid local minima inherent to ICP-based optimization. The ES-ICP algorithm estimates the camera's rotational pose in  $SO(3)$ , leveraging the spherical event map maintained by the mapping module.

Concurrently, the mapping module selectively updates the spherical event map using key frames determined by significant rotational motion (III-E). Unlike existing methods that may suffer from increasing computational burden over time, our mapping strategy employs incremental updates with ikd-Tree and our Regional Density Management to ensure that computational costs remain stable and bounded regardless of sequence length or scene complexity. This updated map not only aids in subsequent tracking iterations but also serves as the basis for panoramic image generation (III-F).

This iterative tracking and mapping process achieves robust high-frequency rotation estimation while maintaining predictable real-time performance.

Tab. II summarizes the key symbols and variables used throughout our methodology.

## B. Event Spherical Representation

In event-based rotational motion estimation, the choice of event representation is crucial for both accuracy and computational efficiency. We propose a spherical representation of events, which offers two significant advantages over traditional pixel-plane approaches: 1) Simplification of rotational motion formula, and 2) Enhanced spatial resolution and mapping within a continuous domain.

1) *Simplified Motion Geometry on Unit Sphere*: In pure rotational motion, considering events on the pixel plane involves a complex series of transformations including rotation, perspective projection, and distortion. Fig. 3 illustrates this process, showing the transformation from a 3D point to its spherical representation. Let's consider a 3D point  $\mathbf{P}_i$  and its projection onto the image plane  $\mathbf{x}_i^I$ . The process can be described as follows [55]:

$$\mathbf{x}_i^I = \mathbf{f}(\mathbf{K}[\mathbf{R}|\mathbf{t}]\mathbf{P}_i) \quad (6)$$

where  $\mathbf{K}$  is the camera intrinsic matrix,  $\mathbf{f}$  is the distortion function, and  $[\mathbf{R}|\mathbf{t}]$  represents the rigid body transformation from the world coordinate system to the camera coordinate system.

Now, consider the same point  $\mathbf{P}_i$  observed from two camera views  $I_1$  and  $I_2$  related by a rotation  $\mathbf{R}_{12}$  (denoting the rotation from reference frame 2 to reference frame 1, and  $\mathbf{t}_{12} = \mathbf{0}$ ). The corresponding pixel coordinates in the two views,  $\mathbf{x}_i^{I_1}$  and  $\mathbf{x}_i^{I_2}$ , are related by:

$$\mathbf{x}_i^{I_1} = \mathbf{f}(\mathbf{K}\mathbf{R}_{12}\mathbf{K}^{-1}\mathbf{f}^{-1}(\mathbf{x}_i^{I_2})) \quad (7)$$

where  $\mathbf{f}^{-1}$  is the undistortion function. This expression, involving multiple non-linear transformations, is both mathematically complex and computationally demanding.

In contrast, on a unit sphere, the projection of a 3D point  $\mathbf{P}_i$  can be expressed as:

$$\mathbf{p}_i^s = \frac{[\mathbf{R}|\mathbf{t}]\mathbf{P}_i}{\|[\mathbf{R}|\mathbf{t}]\mathbf{P}_i\|_2} \quad (8)$$

For pure rotational motion,  $\mathbf{t} = \mathbf{0}$ . Moreover, since  $\mathbf{R}$  is a rotation matrix, its determinant is 1, which preserves the vector's magnitude. Therefore, the equation simplifies to:

$$\mathbf{p}_i^s = \frac{\mathbf{R}\mathbf{P}_i}{\|\mathbf{P}_i\|_2} \quad (9)$$

Consequently, for two spherical projections  $\mathbf{p}_i^{s_1}$  and  $\mathbf{p}_i^{s_2}$  from views differing by a rotation  $\mathbf{R}_{12}$ , we have:

$$\mathbf{p}_i^{s_1} = \mathbf{R}_{12}\mathbf{p}_i^{s_2} \quad (10)$$

This formulation provides a direct and simple representation of rotational motion on the unit sphere, significantly reducing computational complexity compared to the pixel-plane formulation.

2) *Enhanced Spatial Resolution in Continuous Spherical Domain*: While event cameras provide discrete pixel locations, our spherical representation offers significant advantages in spatial resolution and mapping continuity. On the pixel plane, each event is confined to a discrete grid, with each pixel corresponding to a specific field of view (FOV). This discretization

limits the precision of motion estimation, as movements within a single pixel's FOV become indistinguishable.

In contrast, the spherical representation, although derived from discrete pixel data, allows for a more nuanced positioning of events in 3D space. This approach enables us to maintain sub-pixel precision in event positioning, as the spherical coordinates are not confined to a discrete grid. Consequently, we maintain a discretely sampled spherical event map within this continuous domain, where events can be placed at arbitrary positions on the unit sphere. This enhanced spatial resolution is particularly beneficial for representing and tracking small motions, even when they don't result in a change of pixel coordinates.

Fig. 4 illustrates this advantage, showing how a small camera rotation can lead to a detectable change in the spherical representation ( $\Delta\mathbf{p}_i^s$ ), while potentially resulting in no change in the pixel coordinates ( $\Delta\mathbf{x}_i^I = 0$ ). This capability significantly enhances the precision of our rotation estimation algorithm, allowing for more accurate tracking of camera motion.

Given these advantages, we implement the Event Spherical Representation as follows:

Given an event  $e_i = (\mathbf{x}_i^I, t_i, p_i)$ , where  $\mathbf{x}_i^I = (u_i, v_i)^\top$  denotes the pixel coordinates,  $t_i$  the timestamp, and  $p_i$  the polarity, we perform the following steps (illustrated in Fig. 3):

1) **Undistortion**: First, we undistort the pixel coordinates  $\mathbf{x}_i^I$  using the camera's intrinsic parameters and distortion coefficients:

$$\mathbf{x}_i^u = \mathbf{f}^{-1}(\mathbf{x}_i^I) \quad (11)$$

2) **Normalization**: We then normalize the undistorted coordinates using the camera's intrinsic matrix  $\mathbf{K}$ :

$$\mathbf{p}_i^n = \mathbf{K}^{-1} \begin{pmatrix} \mathbf{x}_i^u \\ 1 \end{pmatrix} \quad (12)$$

3) **Spherical Projection**: Finally, we project the normalized coordinates onto the unit sphere:

$$\mathbf{p}_i^s = \frac{\mathbf{p}_i^n}{\|\mathbf{p}_i^n\|_2} \quad (13)$$

The resulting  $\mathbf{p}_i^s$  is a 3D point on the unit sphere, representing the direction of the event in 3D space. This spherical representation allows us to treat events as points on a continuous surface, facilitating more accurate rotational motion estimation.

## C. Event Spherical Frame Formation

The continuous nature of event streams reflects the ongoing motion of the event camera. While contrast maximization methods typically process events over relatively long time windows (e.g., 0.1 s) under the assumption of constant angular velocity, we propose a different approach that operates on much shorter time scales to better handle varying motion patterns. We segment the event stream at a frequency  $f$  and select the first  $n$  events from each segment, as illustrated in Fig. 5. These events are then transformed into spherical coordinates as described in III-B to form event spherical frames.

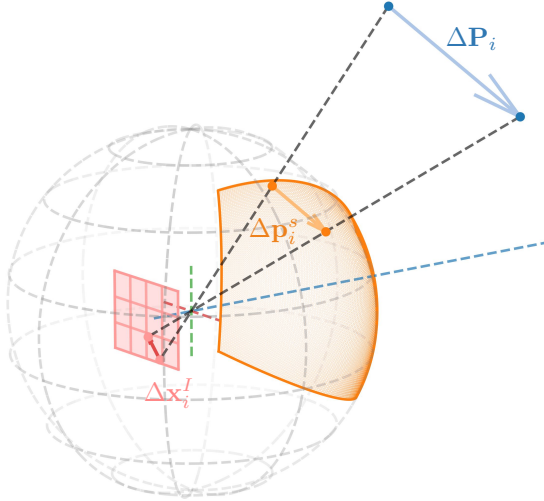


Fig. 4: Illustration of motion sensitivity differences between spherical and pixel representations. When the event camera undergoes a small rotation, the 3D point position relative to the camera changes by  $\Delta P_i$ . This results in a measurable change  $\Delta p_i^s$  on the spherical surface. However, in the pixel coordinate system, the motion may not cause a change in pixel location, resulting in  $\Delta x_i^f = 0$ . This demonstrates the higher sensitivity and continuous nature of the spherical representation compared to the discrete pixel representation.

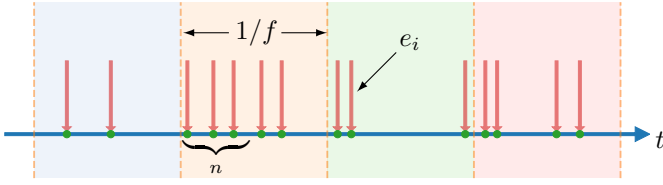


Fig. 5: Event spherical frame formation process: Each downward arrow represents a triggered event  $e_i$ . Colored backgrounds indicate time segments of duration  $1/f$ . The brace underneath shows the selection of the first  $n$  events within each time segment to form an event spherical frame.

To illustrate why our frame selection strategy effectively minimizes intra-frame camera motion, let us analyze a specific example from our implementation on ECRot [40] dataset. For ECRot sequences, we set  $f = 1000$  Hz and  $n = 1500$ . Our analysis shows that these  $n = 1500$  events span an average duration of only 0.121 ms. Taking the average angular velocity of  $\omega = 120^\circ/\text{s}$  as an example, this brief time span results in an intra-frame rotation of  $0.0145^\circ$ , leading to very small motion-induced pixel displacement within each frame. Each frame containing only 1500 events is too sparse to reveal the scene structure, making it challenging for contrast maximization methods to process effectively. However, our ES-ICP algorithm is specifically designed to handle such sparse point clouds effectively. This configuration allows our subsequent ES-ICP method to estimate  $SO(3)$  pose at 1000 Hz.

Although the intra-frame motion is already very small, we further apply motion compensation to the events within each frame to achieve the highest possible accuracy. For each frame, we estimate a constant angular velocity  $\omega$  based on the rotational change between the two most recent pose estimates.

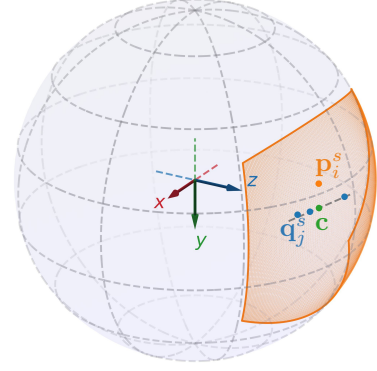


Fig. 6: ES-ICP error visualization. The shaded region represents the spherical event map  $\mathcal{M}^s$ . Our objective is to minimize the distances between all  $p_i^s$  in the current event frame and the line fitted to their  $k$  nearest neighbors  $q_j^s$  in the map. The point  $c$  represents the centroid of the  $k$  nearest neighbors used for line fitting.

Given this short time span (0.121 ms on average), the constant angular velocity assumption is much more reasonable compared to applying it over longer windows. Using this angular velocity, we then warp all events within the frame to the timestamp of the first event in the frame. Specifically, for an event  $e_i$  with timestamp  $t_i$  and its spherical representation  $p_i^s$ , we apply the following transformation:

$$p_i^s \leftarrow \exp((t_0 - t_i)\omega^\wedge) p_i^s \quad (14)$$

where  $t_0$  is the timestamp of the first event in the frame,  $t_i$  is the timestamp of the  $i$ -th event,  $\omega^\wedge$  denotes the skew-symmetric matrix of  $\omega$ , and  $\exp(\cdot^\wedge)$  is the exponential map from  $\mathfrak{so}(3)$  to  $SO(3)$ . After processing all  $n$  events, we obtain the motion-compensated event spherical frame  $\mathcal{E}^s = \{p_k^s\}_{k=0}^{n-1}$ .

#### D. Event Spherical Iterative Closest Point (ES-ICP) Algorithm

The core of our approach lies in the Event Spherical Iterative Closest Point (ES-ICP) algorithm, which is designed to efficiently estimate rotational motion using spherical event representations. As illustrated in Fig. 1b, our goal is to align the sparse event point cloud with a denser spherical event map on the surface of a unit sphere.

Since events are primarily triggered by edges in the environment, and these edges typically form continuous structures on the spherical surface, we optimize the distance between points and nearby line segments rather than point-to-point distances for improved robustness and accuracy. This approach better captures the underlying edge structure of the scene while being more resilient to noise and sparse event distributions. As visualized in Fig. 6, both the map and the frame exist on a curved surface (the unit sphere), where these line segments locally approximate the edge structures projected onto the sphere.

Given a set of event projections on a unit sphere  $\mathcal{E}^s = \{p_i^s\}_{i=0}^{n-1}$ , representing a sparse event spherical frame of  $n$  points, and a spherical event map  $\mathcal{M}^s = \{q_j^s\}_{j=0}^{m-1}$ , which is an accumulated representation of previously aligned event

frames, our objective is to optimize the pose  $\mathbf{R}$  in  $SO(3)$  to minimize the distance between points in  $\mathcal{E}^s$  and  $\mathcal{M}^s$ . This can be formulated as:

$$\mathbf{R}^* = \operatorname{argmin}_{\mathbf{R} \in SO(3)} \sum_{i=0}^{n-1} d(\mathbf{R}\mathbf{p}_i^s, \mathcal{M}^s) \quad (15)$$

where  $d(\cdot, \cdot)$  represents a distance metric and  $\mathbf{R}^*$  is the optimal rotation we seek to estimate.

To implement this approach, for each  $\mathbf{p}_i^s$ , we first apply the current estimate of the rotation matrix  $\mathbf{R} \in SO(3)$ :

$$\tilde{\mathbf{p}}_i^s = \mathbf{R}\mathbf{p}_i^s \quad (16)$$

We then employ a k-d tree structure to efficiently find the  $k = 5$  nearest neighbors of  $\tilde{\mathbf{p}}_i^s$  in  $\mathcal{M}^s$ . Using these neighbors, we fit a line  $l : \mathbf{d}\tau + \mathbf{c}$ , where  $\mathbf{d}$  is the direction vector and  $\mathbf{c}$  is the centroid of the  $k$  nearest neighboring points. We choose  $k = 5$  as it provides sufficient points for robust line fitting while maintaining computational efficiency and focusing on local geometric structure. It's worth noting that while Fig. 6 illustrates this concept with exaggerated distances for clarity, in practice, the nearest neighbors are typically very close to each other on the unit sphere. As a result, the fitted line closely approximates the tangent to the unit sphere at that point.

The optimization problem can then be reformulated as:

$$\mathbf{R}^* = \operatorname{argmin}_{\mathbf{R} \in SO(3)} \sum_{i=0}^{n-1} \|\mathbf{d} \times (\mathbf{R}\mathbf{p}_i^s - \mathbf{c})\|_2^2 \quad (17)$$

We solve this non-linear least squares optimization problem using the Gauss-Newton method. For each point, we derive the Jacobian matrix  $\mathbf{J}_i \in \mathbb{R}^{3 \times 3}$  with respect to the Lie algebra of  $SO(3)$ :

$$\mathbf{J}_i = -\mathbf{d}^\wedge \mathbf{R}\mathbf{p}_i^{s\wedge} \quad (18)$$

where  $\mathbf{d}^\wedge$  and  $\mathbf{p}_i^{s\wedge}$  denote the skew-symmetric matrices of  $\mathbf{d}$  and  $\mathbf{p}_i^s$ , respectively.

In each Gauss-Newton iteration, we construct and solve the normal equation:

$$\mathbf{H}\Delta\mathbf{x} = \mathbf{g} \quad (19)$$

Here,  $\mathbf{H} \in \mathbb{R}^{3 \times 3}$  is the approximated Hessian matrix,  $\Delta\mathbf{x} \in \mathbb{R}^3$  is the incremental update we seek in the Lie algebra  $\mathfrak{so}(3)$ , and  $\mathbf{g} \in \mathbb{R}^3$  is the gradient vector. These are computed as:

$$\mathbf{H} = \sum_{i=0}^{n-1} \mathbf{J}_i^\top \mathbf{J}_i, \quad \mathbf{g} = - \sum_{i=0}^{n-1} \mathbf{J}_i^\top [\mathbf{d} \times (\mathbf{R}\mathbf{p}_i^s - \mathbf{c})] \quad (20)$$

After solving Eq. 19 to obtain the update  $\Delta\mathbf{x}$  in the Lie algebra  $\mathfrak{so}(3)$ , we update the current pose estimate  $\mathbf{R}_{it}$  using the exponential map:

$$\mathbf{R}_{it+1} = \mathbf{R}_{it} \exp(\Delta\mathbf{x}^\wedge) \quad (21)$$

where  $\exp(\cdot^\wedge)$  maps from  $\mathfrak{so}(3)$  to  $SO(3)$ , and  $it$  denotes the iteration number.

The optimization is considered converged when the magnitude of the update  $\|\Delta\mathbf{x}\|$  falls below a predefined threshold or reaches a maximum number of iterations, yielding an optimal rotation estimate that precisely aligns the event frame with the spherical map. A crucial aspect of our ES-ICP implementation is its high-frequency operation at 1000 Hz. This design choice helps mitigate a fundamental challenge inherent to ICP-based algorithms: sensitivity to initialization and susceptibility to

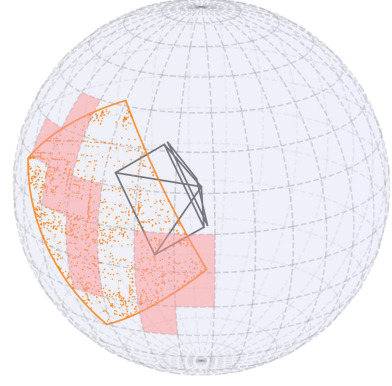


Fig. 7: Illustration of Regional Density Management (RDM) for spherical event representation. The unit sphere is divided into grid cells based on latitude-longitude lines, each with a maximum point capacity. Since grid cells near the poles have smaller surface areas than those at the equator, their maximum point capacity is proportionally scaled according to their surface area. When a new keyframe is added to the spherical map, events are only inserted into regions that haven't reached their capacity limits. As shown in the figure, the pink grid cells have already reached their capacity, so any new points from the keyframe that fall within these saturated regions are not added to the map.

local minima. By operating at such high frequencies, the actual rotation between consecutive frames becomes very small, ensuring that the previous ES-ICP solution provides an excellent initial guess for the current frame. While ICP remains a local optimizer, this strategy significantly improves the likelihood of ES-ICP converging to the correct solution, which is a core reason for EROAM's superior accuracy compared to methods that operate over longer time windows.

### E. Event Spherical Map Maintenance and Update

To maintain an accurate and efficient representation of the environment while ensuring predictable computational costs for real-time operation, we employ an intelligent map maintenance approach that combines incremental updates with regional density control. We selectively update our spherical event map based on significant camera motion, designating certain frames as key frames based on a rotation threshold criterion.

Let  $\mathbf{R}_c$  be the current frame's estimated rotation and  $\mathbf{R}_k$  be the rotation of the last key frame. We consider the current frame as a new key frame if:

$$\|\log(\mathbf{R}_c \mathbf{R}_k^{-1})^\vee\|_2 > \theta_t \quad (22)$$

where  $\log(\cdot)^\vee$  is the logarithm map from  $SO(3)$  to  $\mathfrak{so}(3)$ , and  $\theta_t$  is a predefined rotation threshold. Upon identifying a new key frame, we update our map using an incremental k-d tree (ikd-Tree) data structure [56] and our novel Regional Density Management (RDM) approach. Unlike traditional static k-d trees that require complete rebuilding after updates, the ikd-Tree supports efficient incremental insertions and deletions, allowing us to dynamically update the spherical map without the computational overhead of rebuilding the entire

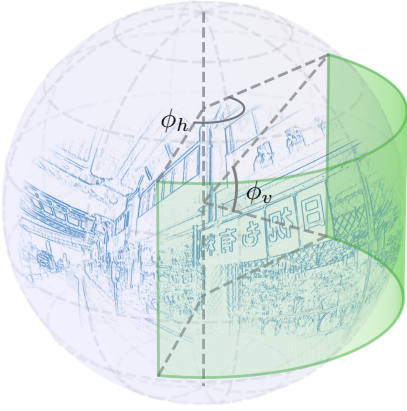


Fig. 8: Projection from spherical event map to panoramic image. Events on the unit sphere are projected onto a surrounding cylinder, then unwrapped to form the panorama.  $\phi_v$ : vertical field of view,  $\phi_h$ : horizontal span angle. The cylinder is discretized based on desired pixel density to generate the final panoramic image.

tree structure. This design choice is fundamental to our real-time performance guarantee, as it ensures that map update operations maintain bounded and predictable execution times regardless of map size or update frequency.

A significant challenge in event-based mapping arises when the camera repeatedly observes the same area, generating redundant points that can degrade performance and increase memory consumption. Our RDM approach addresses this by intelligently controlling point density across the spherical surface while maintaining stable computational complexity. As illustrated in Fig. 7, RDM partitions the unit sphere into grid cells based on latitude-longitude lines, each with a maximum point capacity. Since grid cells near the poles have smaller surface areas than those at the equator, their maximum point capacity is proportionally scaled according to their surface area. When a new keyframe is added to the spherical map, events are only inserted into regions that haven't reached their capacity limits. The pink grid cells in the figure have already reached their capacity, so any new points from the keyframe that fall within these saturated regions are not added to the map.

This density management mechanism maintains a uniform spatial density across the map, preventing over-representation of frequently observed regions while preserving structural details and feature richness. Crucially, RDM ensures that computational costs remain bounded and predictable throughout extended operation, as the maximum number of points in the map is inherently limited by the grid structure. The combination of ikd-Tree and RDM creates a spherical map that dynamically evolves as the camera explores the environment, efficiently balancing computational resources with geometric integrity while guaranteeing the stable execution times essential for real-time operation.

#### F. Panoramic Image Generation

A valuable byproduct of our system is the generation of panoramic images. To generate these panoramic representations, we utilize all aligned event spherical frames, which are

accumulated in a dedicated buffer throughout the system's operation. The conversion process involves projecting the events from the unit sphere onto a surrounding cylinder, which is then unwrapped to form a 2D panoramic representation, as illustrated in Fig. 8. The projection process is defined by two key parameters:  $\phi_v$ , the vertical field of view, which determines the height of the cylindrical projection surface, and  $\phi_h$ , the horizontal span angle, which defines the width of the panoramic image. Fig. 1c shows an example of the resulting panoramic image generated by our method.

The conversion from spherical coordinates to panoramic image coordinates involves projecting each spherical point  $\mathbf{p}_i^s = (x, y, z)^T$  onto the cylinder surface using the equation:

$$\mathbf{p}_i^c = \left( \frac{x}{\sqrt{x^2 + y^2}}, \frac{y}{\sqrt{x^2 + y^2}}, \frac{z}{\sqrt{x^2 + y^2}} \right)^T \quad (23)$$

This projection normalizes the x and y coordinates to the unit circle while preserving the relative height of z. The cylinder surface is then discretized based on the desired pixel density of the panoramic image, with the azimuthal angle of the projected point determining its horizontal position and its height on the cylinder determining its vertical position in the image.

A key advantage of our approach is that the entire mapping process operates in continuous spherical space, maintaining complete independence from any discretization requirements. Unlike traditional methods that require predefined resolutions, our method allows for the generation of panoramic images at arbitrary resolutions as needed, with the panorama generation process entirely decoupled from the core tracking and mapping pipeline. This design choice offers several benefits:

- The spherical mapping and pose estimation operate in continuous space, ensuring their accuracy is independent of any discretization choices.
- Multiple panoramic images can be generated at different resolutions without modifying the underlying map data.
- The panorama generation serves as an independent post-processing step, preserving the real-time performance of the core system.

## IV. EXPERIMENTS

In this section, we present a comprehensive evaluation of our proposed event-based rotational motion estimation method. We begin by detailing our experimental setup, including evaluation metrics, datasets, and hardware configuration (IV-A). We then evaluate our method on both synthetic and real-world data: first on the ECRot dataset (IV-B), followed by extended simulations using ESIM (IV-C) to assess performance under various challenging conditions, and then on real-world sequences (IV-D). We provide runtime analysis (IV-E), evaluate robustness to unmodeled translation (IV-F), and conduct ablation studies (IV-G).

### A. Experimental Setup

1) *Evaluation Metrics*: To rigorously assess the performance of our proposed method, we employ two primary metrics for evaluating rotational motion estimation accuracy: Absolute Pose Error (APE) [57] and Relative Pose Error (RPE)

[57]. These metrics provide a comprehensive evaluation of both global consistency and local accuracy of the estimated camera rotations.

a) *Absolute Pose Error (APE)*: The APE measures global pose consistency. For timestamp  $t_k$ , the absolute rotation error is:

$$\epsilon_k = \log(\mathbf{R}'_k{}^\top \mathbf{R}_k)^\vee \quad (24)$$

where  $\mathbf{R}_k$  and  $\mathbf{R}'_k$  are estimated and ground truth rotations, and  $\|\epsilon_k\|_2$  represents the angular error.

To obtain a single representative value, we calculate the mean of these angular errors over all timestamps:

$$\overline{ape} = \frac{1}{N} \sum_{k=1}^N \|\epsilon_k\|_2 \quad (25)$$

where  $N$  is the total number of timestamps in the evaluated trajectory. This mean value  $\overline{ape}$  provides an average measure of the angular error across the entire trajectory.

b) *Relative Pose Error (RPE)*: The RPE measures the local accuracy of the pose estimates by comparing the relative rotation between two timestamps in the estimated trajectory to the corresponding relative rotation in the ground truth trajectory. For a pair of timestamps  $t_k$  and  $t_{k+\Delta}$ , the relative rotation error  $\delta_k$  is calculated as:

$$\delta_k = \log\left(\left(\mathbf{R}'_k{}^\top \mathbf{R}'_{k+\Delta}\right)^{-1} \left(\mathbf{R}_k{}^\top \mathbf{R}_{k+\Delta}\right)\right)^\vee \quad (26)$$

where  $\{\mathbf{R}_k, \mathbf{R}_{k+\Delta}\}$  and  $\{\mathbf{R}'_k, \mathbf{R}'_{k+\Delta}\}$  are pairs of estimated and ground truth poses, respectively. Similar to the APE, the magnitude of  $\delta_k$ , denoted as  $\|\delta_k\|_2$ , represents the angular difference between the estimated and ground truth relative rotations.

The mean of these relative rotation errors  $\overline{rpe}$  is then computed as:

$$\overline{rpe} = \frac{1}{M} \sum_{k=1}^M \|\delta_k\|_2 \quad (27)$$

where  $M$  is the total number of relative pose pairs evaluated along the entire trajectory. To ensure fair comparison across methods with different estimation frequencies, we compute the RPE at fixed intervals corresponding to  $10^\circ$  of rotation in the ground truth trajectory. An  $\overline{rpe}$  value of  $0.5^\circ$  indicates that estimated relative rotations over  $10^\circ$  intervals differ from ground truth by  $0.5^\circ$  on average, providing consistent local accuracy measurement across methods.

For the evaluation of APE and RPE across all experiments, we utilize the EVO toolkit [58], a software package designed for the evaluation of odometry and SLAM algorithms, ensuring consistent and reproducible assessments. To facilitate intuitive understanding of the error magnitudes, we convert all radian measurements to degrees in our reported results.

2) *Datasets*: To comprehensively evaluate our method's accuracy and robustness in rotation estimation, we utilize four types of data sources: the ECRot synthetic dataset [40], extended simulations generated using the ESIM simulator [59], the Event Camera Dataset (ECD) [60], and our newly collected real-world sequences with LiDAR-based ground truth. Further details on their motion patterns, including event rates and average angular velocities ( $\omega_{avg}$ ), are provided in Tab. VII and Tab. VIII.

a) *ECRot Synthetic Dataset*: We utilize all six synthetic sequences from the ECRot dataset: bay, bicycle, city, street, town and playroom. The first five sequences feature a resolution of  $240 \times 180$  with a duration of 5 s, while the playroom sequence has a resolution of  $128 \times 128$  and spans 2.5 s. Each sequence provides events and ground truth poses for quantitative evaluation.

b) *Extended ESIM Simulations*: Given the relatively short duration and moderate motion patterns in the ECRot dataset, we generate additional sequences using ESIM to evaluate our method under more challenging conditions, including various sequence durations (10–80 s) and different angular velocities ( $49.83$ – $393.21^\circ/\text{s}$ ).

c) *Real-World Sequences*: We collected 16 real-world sequences using a synchronized setup consisting of an iniVation DVXplorer event camera ( $640 \times 480$  resolution) and a Livox Avia LiDAR. The two sensors are hardware-synchronized, and their extrinsic parameters are calibrated using the edge-based calibration method proposed in [61]. Among these sequences, the limx-rotation and limx-sway sequences were specifically collected using our LimX TRON 1 wheeled bipedal robot equipped with an iniVation DVXplorer event camera, as shown in Fig. 20a. Ground truth camera trajectories are derived by combining high-precision LiDAR poses from Point-LIO [62] with the calibrated LiDAR-event camera extrinsic parameters, providing accurate benchmarks for evaluating our rotation estimation results.

d) *Event Camera Dataset (ECD)*: To evaluate robustness to unmodeled translational motion, we use the ECD [60], which features unconstrained handheld 6-DOF motion with translation typically within  $\sim 0.3$  m. Following CMax-SLAM's protocol [40], we process four sequences (boxes, dynamic, poster, shapes), using the first 30 seconds of each.

3) *Hardware Configuration*: To ensure consistency and fair comparison across all experiments, we conducted our evaluations on a single laptop computer. The hardware configuration consists of an Intel Core i9-14900HX CPU, 32GB of RAM, and an NVIDIA RTX 4060 GPU.

## B. Experiments on ECRot Dataset

We conducted experiments using all six synthetic sequences from the ECRot dataset [40], comparing our method with several state-of-the-art approaches. Tab. III presents the quantitative results of our method compared to these approaches including SMT [38], RTPT [39], CM-GAE [41], and CMax-SLAM [40].

Among all methods tested, none of them except CMax-SLAM and our EROAM demonstrated consistent performance. SMT, despite utilizing ground truth initialization to construct its initial map, fails to maintain stable pose estimation and quickly deviates from the initialized state, resulting in complete failure on all sequences. Moreover, SMT exhibits the highest computational overhead in our experiments. All other evaluated methods, including RTPT, CM-GAE, CMax-SLAM, and our EROAM, operate without requiring any prior pose information.

RTPT demonstrates better performance than SMT, maintaining tracking during initial camera rotations. However, it

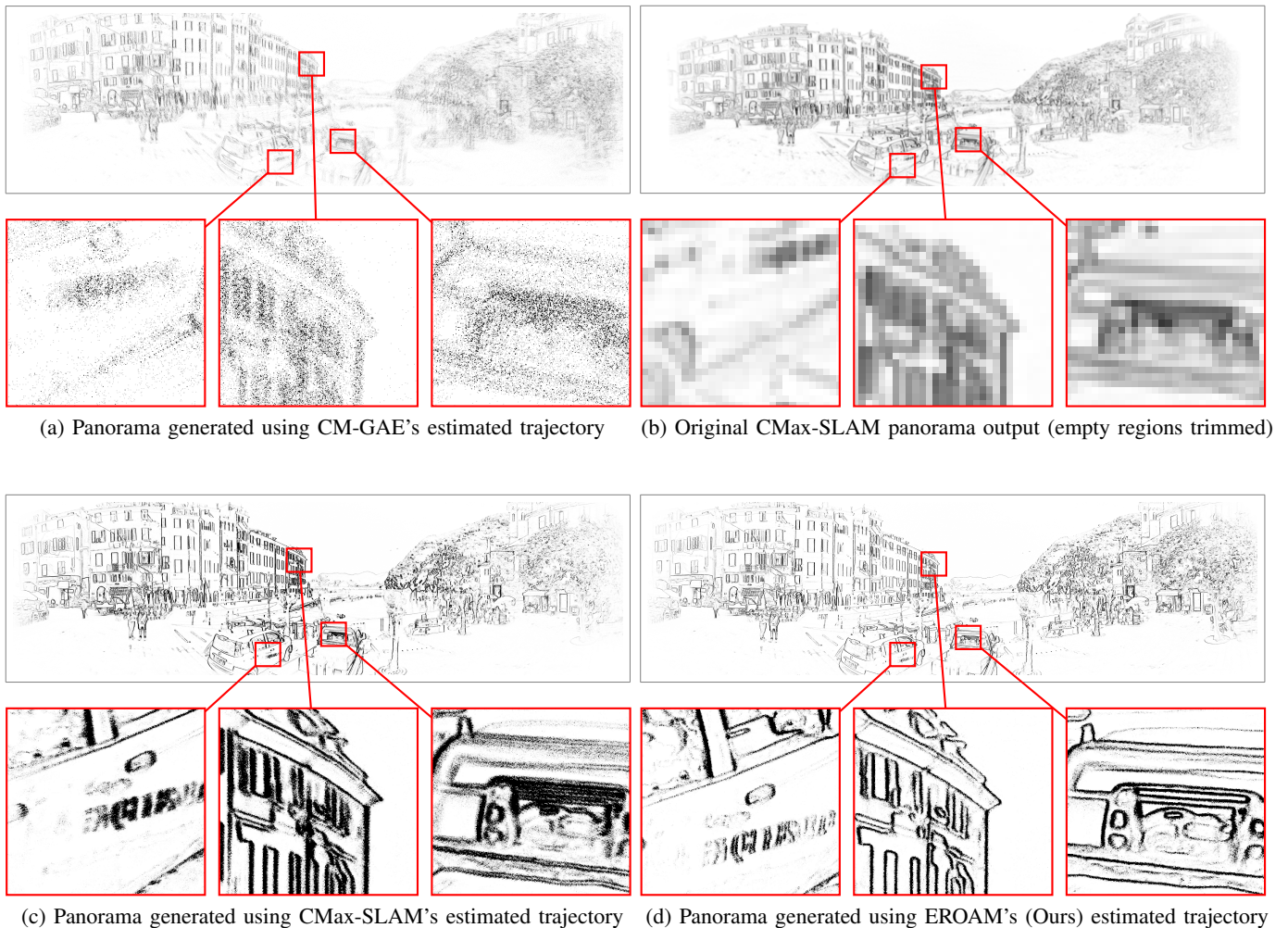


Fig. 9: Qualitative comparison of panoramic mapping results on the `town` sequence from ECRot dataset [40]. (a,c,d) show panoramas generated using our unified pipeline ( $7617 \times 2000$  resolution) with different methods’ estimated trajectories, where identical event window size (0.2 ms) and colorization scheme are applied. (b) shows the original panorama output from CMax-SLAM’s implementation for reference. The zoomed-in regions highlight that our method produces sharper edges and clearer structural details compared to other approaches.

TABLE III: Comparison of rotational motion estimation accuracy on ECRot [40] synthetic datasets.

Sequence	bay [40]		bicycle [40]		city [40]		street [40]		town [40]		playroom [40]	
	$\overline{ape}$ (°)	$\overline{rpe}$ (°)										
SMT [38]	-	-	-	-	-	-	-	-	-	-	-	-
RTPT [39]	-	-	-	-	-	-	-	-	-	-	-	-
CM-GAE [41]	-	-	0.856	0.244	-	-	-	-	2.600	0.603	3.684	0.823
CMax-SLAM [40]	0.802	0.141	0.727	0.098	1.113	0.294	0.517	0.181	1.238	0.130	0.727	<b>0.095</b>
EROAM (ours)	<b>0.239</b>	<b>0.062</b>	<b>0.159</b>	<b>0.076</b>	<b>0.111</b>	<b>0.083</b>	<b>0.166</b>	<b>0.093</b>	<b>0.342</b>	<b>0.117</b>	<b>0.311</b>	0.150

“-” indicates a failure case where after multiple attempts, the method still either produces  $\overline{ape}$  larger than  $20^\circ$ , crashes during execution, or outputs undefined quaternions.

ultimately fails to process complete sequences despite multiple parameter tuning attempts, confirming the limitations reported in [40]. This failure occurs when the camera’s field of view (FOV) approaches the map boundaries - RTPT’s projection mechanism cannot effectively update the map in these situations, and attempts to increase the map size result in insufficient gradient information due to sparse projections.

CM-GAE showed inconsistent performance - we report its best results after multiple parameter tuning attempts, with successful processing of only the bicycle, town, and playroom

sequences, though its performance remains unstable. These three methods demonstrate limited general applicability.

In contrast, both CMax-SLAM and our method successfully processed all six sequences. CMax-SLAM achieved this using their recommended sequence-specific parameters, while our method produced superior results using consistent parameters across all sequences, as evidenced by the lower  $\overline{ape}$  and  $\overline{rpe}$  values. We provide more detailed comparisons between CMax-SLAM and our method in IV-C and IV-E, where we evaluate performance under more challenging conditions and analyze

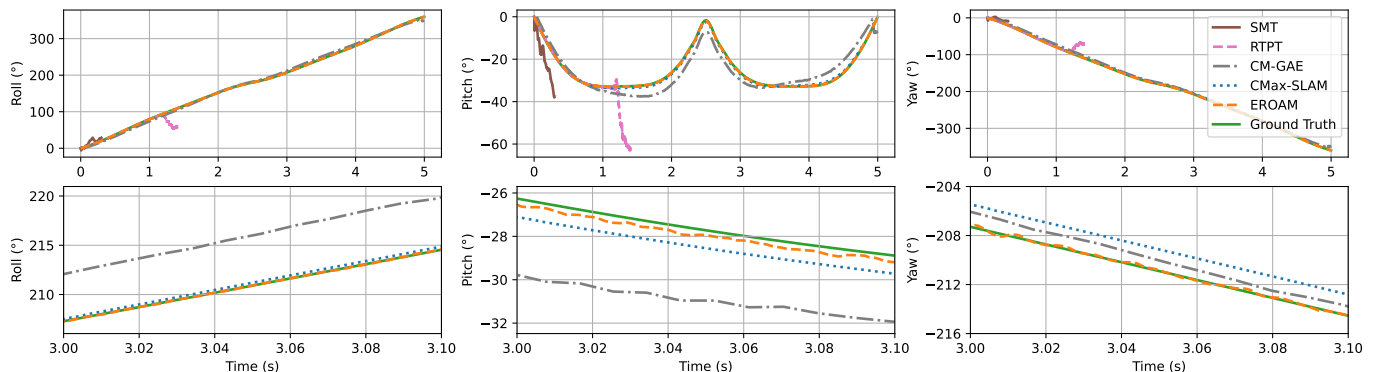


Fig. 10: Rotation estimation results on the `town` sequence from ECRot dataset. The top row shows the full trajectories of roll, pitch, and yaw angles, while the bottom row shows the zoomed-in views from 3.00 s to 3.10 s. Our method (EROAM) achieves comparable accuracy with the ground truth, demonstrating robust rotation estimation performance. The trajectories of SMT and RTPT are truncated after significant deviation from ground truth for better visualization clarity.

TABLE IV: Quantitative comparison of rotational state estimation under increasing angular velocities.

Sequence	DM-1		DM-2		DM-3		DM-4		DM-5		DM-6		DM-7		DM-8	
	$\overline{ape}$ (°)	$\overline{rpe}$ (°)														
CMax-SLAM [40]	0.947	0.174	1.032	0.189	35.927	1.054	114.962	2.040	115.238	1.627	120.625	1.585	100.548	1.341	87.440	1.326
EROAM (ours)	<b>0.139</b>	<b>0.155</b>	<b>0.192</b>	<b>0.093</b>	<b>0.333</b>	<b>0.078</b>	<b>0.237</b>	<b>0.119</b>	<b>0.307</b>	<b>0.091</b>	<b>0.731</b>	<b>0.111</b>	<b>0.300</b>	<b>0.116</b>	<b>0.176</b>	<b>0.105</b>

computational efficiency.

To visualize the detailed performance differences, we present the rotation estimation results on the `town` sequence in Fig. 10. The figure shows both complete trajectories and zoomed-in views of roll, pitch, and yaw angles. SMT and RTPT quickly deviate from the ground truth and fail. CM-GAE maintains tracking but exhibits noticeable drift across all angles. In contrast, our method closely tracks the ground truth trajectory across all three rotation angles, with CMax-SLAM showing similar but slightly less accurate performance, particularly visible in the detailed views.

For qualitative evaluation, we focus on panoramic mapping results from CM-GAE, CMax-SLAM, and our method, as shown in Fig. 9. While CMax-SLAM’s original implementation generates panoramas at a fixed resolution of  $1024 \times 512$  (shown in Fig. 9b, with empty regions trimmed), our mapping framework operates in continuous spherical space rather than discrete panoramic space (detailed in III-F). This continuous representation enables panorama generation at arbitrary resolutions - for this comparison, we chose a resolution of  $7617 \times 2000$  to demonstrate the capability of our method.

To ensure fair visual comparison, we implement a unified panorama generation framework using each method’s estimated trajectories. Fig. 9a, Fig. 9c, and Fig. 9d show panoramas generated using identical parameters: an event window size of 0.2 ms and consistent colorization scheme where the 90th percentile of event counts maps to intensity 255. All three methods’ panoramas are regenerated using their respective estimated trajectories through this unified pipeline.

As evident from the zoomed-in regions in Fig. 9, our method produces panoramic images with significantly sharper edges and clearer structural details compared to other approaches. The improved quality is particularly noticeable in architectural features and text regions, demonstrating the benefits of our

accurate rotation estimation.

### C. Extended Simulation Analysis

While both CMax-SLAM and EROAM successfully process all ECRot sequences, these sequences are short (5s) and exhibit moderate motion patterns, as shown in Fig. 10. For reference, the ECRot `bicycle` sequence has an average angular velocity of  $84.208^\circ/\text{s}$  and acceleration of  $101.73^\circ/\text{s}^2$ . To evaluate the generality and robustness of our method, we conducted extended simulation experiments using ESIM [59] with the `bicycle` scene from ECRot dataset under more challenging conditions.

As shown in Fig. 11a, we designed two sets of sequences to test different aspects: (1) sequences with increasing angular velocities and accelerations (DM-1–DM-8), and (2) sequences of increasing duration (LD-10–LD-80). For the dynamic motion sequences, we progressively increased the magnitude and frequency of rotational motion while maintaining the 5s duration, with angular velocity ranging from  $49.83^\circ/\text{s}$  to  $393.21^\circ/\text{s}$  and angular acceleration from  $70.41^\circ/\text{s}^2$  to  $1121.32^\circ/\text{s}^2$ . For the duration test sequences, we used a moderate dynamic profile (average angular velocity:  $107.24^\circ/\text{s}$ , average angular acceleration:  $200.93^\circ/\text{s}^2$ ) and varied the sequence length from 10s to 80s.

Tab. IV and Fig. 11b present the performance comparison under different angular velocities. While both methods perform well under moderate motion (DM-1 and DM-2,  $\overline{ape} \leq 1.032^\circ$ ), CMax-SLAM’s performance degrades significantly when angular velocity increases (DM-4 onwards), with  $\overline{ape}$  exceeding  $100^\circ$  in high-velocity scenarios. This degradation stems from a fundamental limitation of the contrast maximization framework: it assumes constant angular velocity within each time window used for estimation. Under high-dynamic motions with large angular accelerations, this assumption

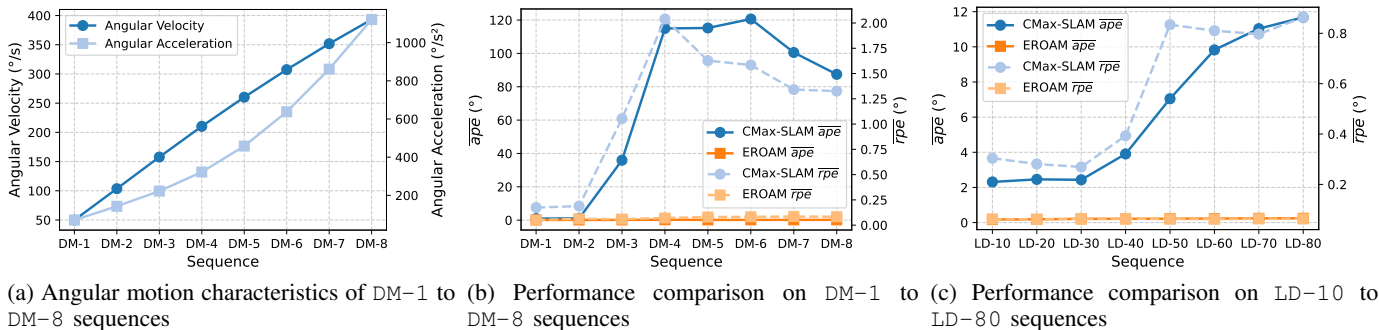


Fig. 11: Quantitative evaluation results. (a) Shows the angular velocity ( $49.83^\circ/\text{s}$  to  $393.21^\circ/\text{s}$ ) and acceleration ( $70.41^\circ/\text{s}^2$  to  $1121.32^\circ/\text{s}^2$ ) characteristics of DM-1 to DM-8 sequences (each 5 s long). (b) Compares the  $\overline{ape}$  and  $\overline{rpe}$  metrics across DM-1 to DM-8 sequences with increasing angular velocities. (c) Compares the  $\overline{ape}$  and  $\overline{rpe}$  metrics for LD-10 to LD-80 sequences of increasing durations (10 s to 80 s).

TABLE V: Assessment of long-term estimation stability across sequences of increasing duration.

Sequence	LD-10		LD-20		LD-30		LD-40		LD-50		LD-60		LD-70		LD-80	
	$\overline{ape}$ (°)	$\overline{rpe}$ (°)														
CMax-SLAM [40]	2.312	0.304	2.460	0.281	2.434	0.269	3.905	0.393	7.047	0.834	9.824	0.810	11.033	0.797	11.677	0.863
EROAM (ours)	<b>0.131</b>	<b>0.083</b>	<b>0.128</b>	<b>0.078</b>	<b>0.133</b>	<b>0.083</b>	<b>0.115</b>	<b>0.129</b>	<b>0.121</b>	<b>0.106</b>	<b>0.120</b>	<b>0.102</b>	<b>0.126</b>	<b>0.082</b>	<b>0.119</b>	<b>0.095</b>

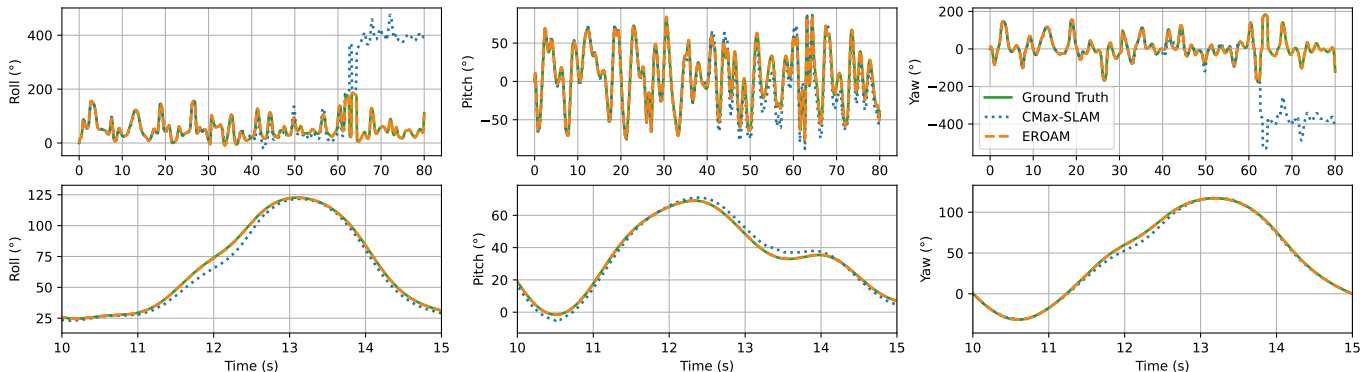


Fig. 12: Comparison of rotational state estimation on the LD-80 sequence. The top row shows the complete 80 s trajectories for roll, pitch, and yaw angles, where CMax-SLAM exhibits significant consistency issues and deviates from ground truth starting from 40 s. The bottom row presents detailed views between 10 s and 15 s, revealing that CMax-SLAM’s estimation already shows noticeable errors even in this early stage. In contrast, EROAM maintains consistent accuracy throughout the entire sequence, closely aligning with ground truth in both global and local perspectives.

becomes invalid, leading to significant estimation errors. Although CMax-SLAM employs backend optimization, it cannot recover from these fundamental front-end estimation errors. This is clearly demonstrated in Fig. 13, where CMax-SLAM’s panoramic reconstruction shows severe ghosting artifacts and double edges due to incorrect motion estimation under high angular velocities.

The comparison across different sequence durations, shown in Tab. V and Fig. 11c, reveals similar patterns. CMax-SLAM exhibits increasing drift as sequence length grows, with  $\overline{ape}$  rising from  $2.312^\circ$  in LD-10 to  $11.677^\circ$  in LD-80. This drift accumulation is clearly visualized in Fig. 12, where CMax-SLAM’s estimated trajectory shows significant deviation from ground truth, particularly after 40 s. This further demonstrates how initial estimation errors in the contrast maximization framework propagate over time, despite backend optimization attempts. In contrast, our method maintains consistent accuracy across all sequences, as our ES-ICP approach directly

optimizes geometric constraints on the unit sphere without relying on assumptions about constant angular velocity.

These results demonstrate that our method not only achieves higher accuracy but also maintains consistent performance under challenging conditions where CMax-SLAM struggles, suggesting superior robustness and general applicability.

#### D. Experiments on Real-World Data

To validate our method’s performance in real-world scenarios, we collected and evaluated EROAM on our EROAM-campus dataset. The dataset contains 16 sequences captured using a custom-built synchronized sensor suite, consisting of an iniVation DVXplorer event camera ( $640 \times 480$  resolution) and a Livox Avia LiDAR mounted on a tripod. Both sensors were hardware-synchronized, and their extrinsic parameters were calibrated using the edge-based calibration method proposed in [61], [63]. We manually performed arbitrary 3-DoF rotational motions while recording data, and obtained ground

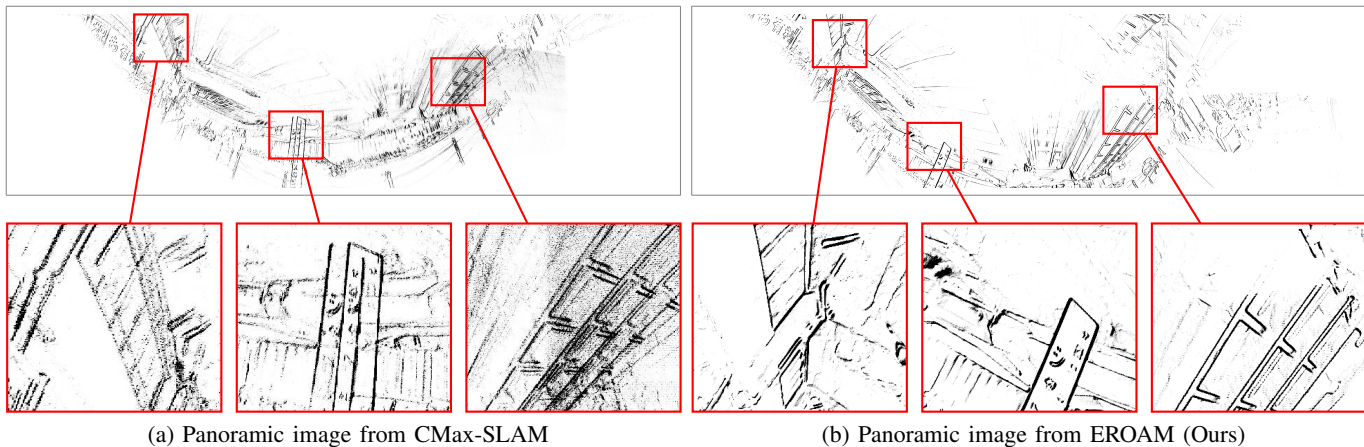


Fig. 13: Qualitative comparison of panoramic mapping results on the DM-4 sequence with high angular velocity. CMax-SLAM’s result exhibits significant ghosting artifacts and double edges in structures, indicating severe rotation estimation errors under high-dynamic motion. These artifacts are particularly visible in the zoomed-in regions, where single structures appear multiple times due to inconsistent motion estimates. In contrast, EROAM produces a panorama with sharp details and precisely aligned structures, demonstrating accurate rotation estimation throughout the sequence.

TABLE VI: Comparison of rotational motion estimation accuracy on EROAM-campus datasets.

Sequence	canteen-entrance		distant-building		embankment-360		embankment		lawn-360		lawn		lecture-hall		front-gate	
	$\overline{ape}$ (°)	$\overline{rpe}$ (°)														
SMT [38]	-	-	-	-	-	-	-	-	-	-	-	-	-	-	-	-
RTPT [39]	-	-	-	-	-	-	0.654	0.403	-	-	-	-	-	-	-	-
CM-GAE [41]	0.688	0.371	5.915	0.899	4.727	0.729	3.228	0.424	7.776	0.670	-	-	3.103	0.407	-	-
CMax-SLAM [40]	0.662	0.557	5.958	1.312	-	-	4.658	2.298	8.733	0.691	-	-	0.518	0.457	13.549	1.227
EROAM (ours)	<b>0.489</b>	<b>0.295</b>	<b>0.239</b>	<b>0.247</b>	<b>1.450</b>	<b>0.231</b>	<b>0.499</b>	<b>0.233</b>	<b>1.248</b>	<b>0.356</b>	<b>0.490</b>	<b>0.208</b>	<b>0.241</b>	<b>0.186</b>	<b>0.475</b>	<b>0.244</b>

Sequence	rooftop		window-building		carpark		condo		crossroad		vehicle		limx-rotation		limx-sway	
	$\overline{ape}$ (°)	$\overline{rpe}$ (°)														
SMT [38]	-	-	-	-	-	-	-	-	-	-	-	-	-	-	-	-
RTPT [39]	-	-	-	-	-	-	-	-	-	-	-	-	-	-	-	-
CM-GAE [41]	14.063	0.695	10.954	1.227	16.567	1.076	19.126	2.430	-	-	-	-	-	-	-	-
CMax-SLAM [40]	0.841	0.406	8.201	4.698	-	-	-	-	-	-	6.119	0.891	14.473	1.412	1.141	0.549
EROAM (ours)	<b>0.438</b>	<b>0.208</b>	<b>0.256</b>	<b>0.167</b>	<b>0.612</b>	<b>0.222</b>	<b>0.543</b>	<b>0.280</b>	<b>0.539</b>	<b>0.204</b>	<b>0.666</b>	<b>0.291</b>	<b>1.720</b>	<b>0.939</b>	<b>0.684</b>	<b>0.426</b>

“-” indicates a failure case where after multiple attempts, the method still either produces  $\overline{ape}$  larger than 20°, crashes during execution, or outputs undefined quaternions.

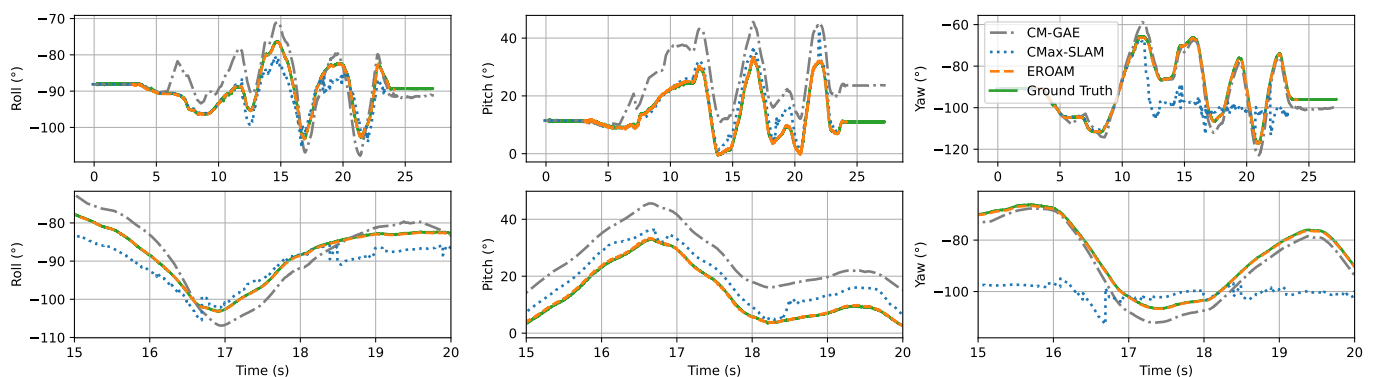


Fig. 14: Comparison of rotational state estimation on the window-building sequence. The top row shows the complete trajectories for roll, pitch, and yaw angles, while the bottom row presents detailed views between 15s and 20s. Our method (EROAM) maintains accurate tracking throughout the sequence, closely following the ground truth trajectory, while CM-GAE and CMax-SLAM show noticeable deviations, particularly evident in the zoomed-in views.

truth camera trajectories by combining high-precision LiDAR poses from Point-LIO [62] with the calibrated LiDAR-event camera extrinsic parameters.

The quantitative comparison results across all sixteen se-

quences are presented in Tab. VI. SMT fails to process any of the sequences, despite multiple parameter tuning attempts. RTPT shows very limited success, only managing to process the embankment sequence with an  $\overline{ape}$  of 0.654°, but

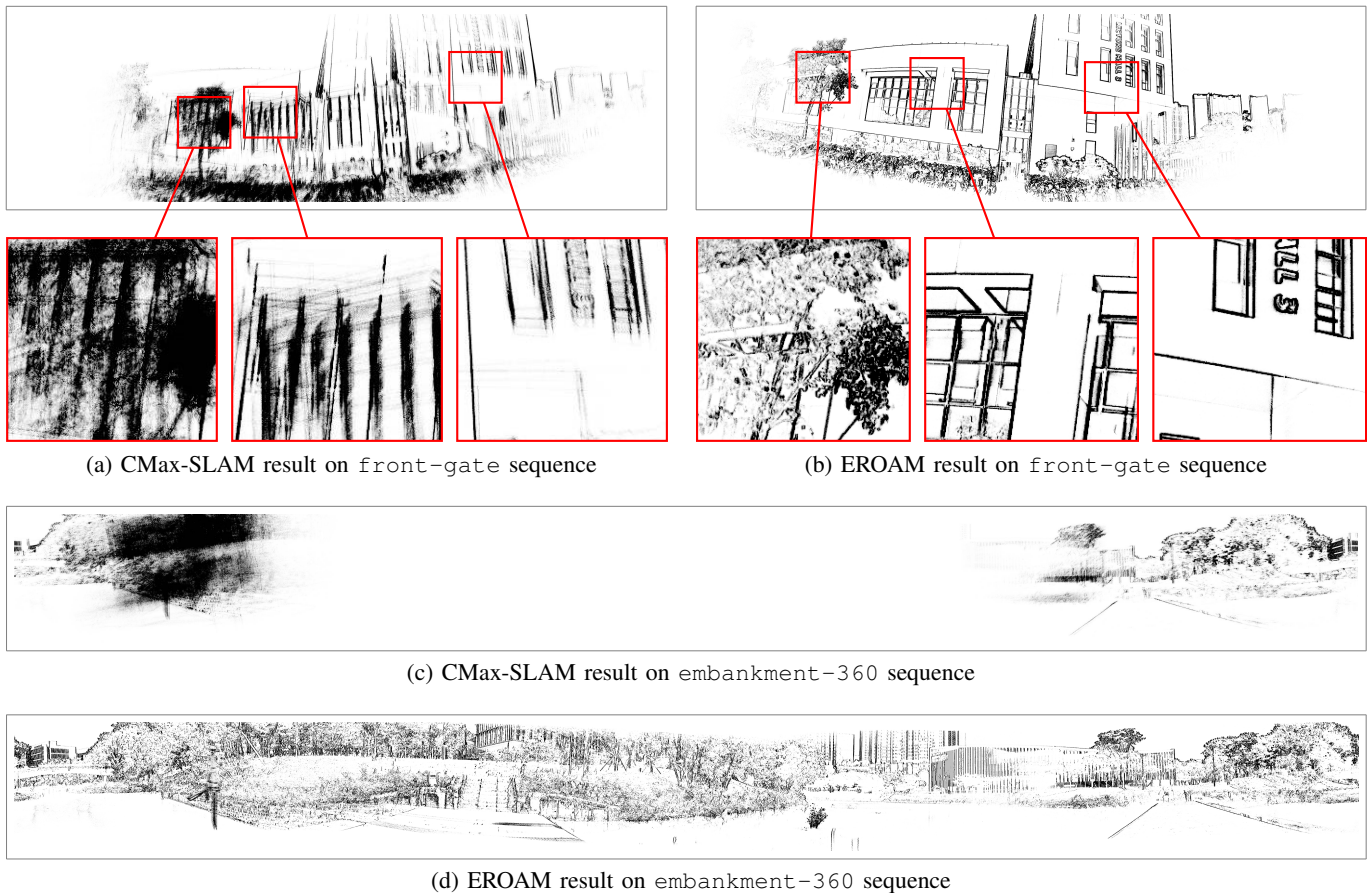


Fig. 15: Qualitative comparison of panoramic mapping results on real-world sequences. The zoomed-in regions in (a,b) highlight the superior structural clarity achieved by our method compared to CMax-SLAM’s results with ghosting artifacts. The full 360° panoramas in (c,d) demonstrate EROAM’s ability to maintain consistent reconstruction quality across extended views.

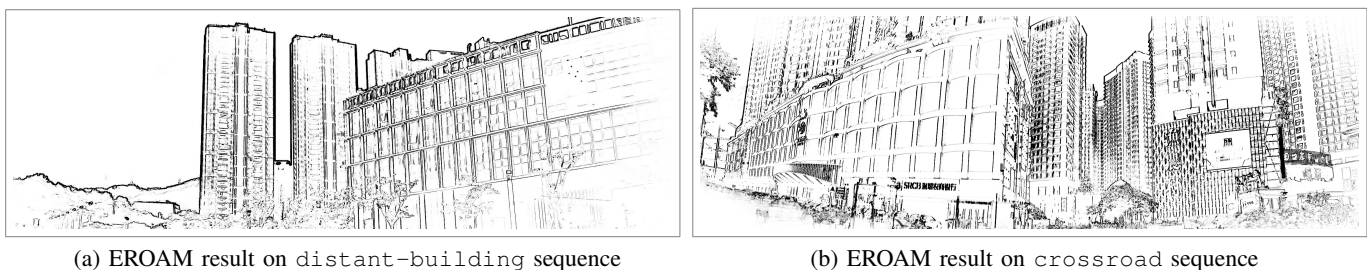


Fig. 16: Additional visualization results from EROAM on different sequences.

failing on all other sequences. CM-GAE and CMax-SLAM demonstrate significant limitations, with CM-GAE exhibiting large estimation errors ( $\overline{ape} > 20^\circ$ ) on 6 out of 16 sequences and CMax-SLAM failing on 5 sequences with  $\overline{ape} > 20^\circ$ . Even on the sequences where these methods do not completely fail, they still exhibit significantly higher errors compared to our method, with  $\overline{ape}$  up to  $19.126^\circ$ .

In contrast, EROAM successfully processes all sequences while maintaining superior accuracy. Our method achieves the lowest error rates across all sequences, with  $\overline{ape}$  below  $1.0^\circ$  in the vast majority of sequences. Even in challenging large-angle motion scenarios, such as the limx-rotation

sequence where the LimX TRON1 robot performs over 3 full rotations, EROAM still demonstrates excellent performance with  $\overline{ape} = 1.720^\circ$  and  $\overline{rpe} = 0.939^\circ$ .

Our method demonstrates particular robustness in challenging real-world scenarios. In sequences containing dynamic objects such as pedestrians, motorcycles, and vehicles (carpark, crossroad, vehicle), EROAM maintains excellent performance thanks to our Regional Density Management (RDM) approach, which prevents the continuous accumulation of events from moving objects into the spherical map. Additionally, EROAM shows consistent accuracy on data collected from our actual robotic platform, with the

TABLE VII: Runtime comparison on ECRot sequences.

Sequence	Duration (s)	Event Rate ( $\times 10^6 \text{ev/s}$ )	$\omega_{\text{avg}}$ ( $^\circ/\text{s}$ )	Runtime (s)			
				RTPT [39]	CM-GAE [41]	CMax-SLAM [40]	EROAM (ours)
bay	5.000	12.357	84.208	67.245	114.744	262.272	<b>4.996</b>
bicycle	5.000	3.716	84.208	35.620	9.283	63.632	<b>4.996</b>
city	5.000	15.026	84.208	79.172	151.906	336.170	<b>4.995</b>
street	5.000	10.385	84.208	56.532	117.441	197.090	<b>4.997</b>
town	5.000	11.074	84.208	62.541	68.969	194.032	<b>4.996</b>
playroom	2.500	1.451	154.746	3.785	<b>2.423</b>	18.987	2.538

TABLE VIII: Runtime comparison on EROAM-campus sequences.

Sequence	Duration (s)	Event Rate ( $\times 10^6 \text{ev/s}$ )	$\omega_{\text{avg}}$ ( $^\circ/\text{s}$ )	Runtime (s)			
				RTPT* [39]	CM-GAE [41]	CMax-SLAM [40]	EROAM (ours)
canteen-entrance	19.590	6.865	62.115	200.557	441.424	520.178	<b>19.578</b>
distant-building	29.196	2.650	63.060	97.019	191.737	386.502	<b>29.208</b>
embankment	31.413	3.473	64.870	166.443	196.604	552.528	<b>31.449</b>
embankment-360	18.101	6.233	97.792	174.606	181.257	782.102	<b>18.125</b>
lawn	47.169	13.802	77.099	-	1318.581	2553.260	<b>47.158</b>
lawn-360	16.090	8.888	83.732	226.574	347.039	558.310	<b>16.079</b>
lecture-hall	18.368	4.064	50.790	99.170	915.236	256.658	<b>18.366</b>
front-gate	26.153	7.300	80.189	294.268	270.939	794.393	<b>26.148</b>
rooftop	50.267	4.349	64.182	321.165	410.770	845.354	<b>50.338</b>
window-building	27.514	9.304	54.567	335.886	877.523	1417.175	<b>27.508</b>
carpark	38.878	9.751	77.642	486.052	780.133	1108.190	<b>38.877</b>
condo	49.389	12.077	76.176	-	988.569	1663.687	<b>49.370</b>
crossroad	44.512	11.171	74.227	664.389	820.304	1342.736	<b>44.502</b>
vehicle	36.043	14.673	85.943	647.659	883.591	1203.566	<b>36.032</b>
limx-rotation	22.090	16.188	106.683	479.243	606.214	695.631	<b>21.988</b>
limx-sway	19.990	17.438	113.613	407.918	754.939	715.156	<b>19.978</b>

\*RTPT fails to process the lawn and condo sequences due to their large size.

limx-rotation and limx-sway sequences captured using the LimX TRON 1 wheeled bipedal robot demonstrating reliable rotation estimation even under the vibrations and motion patterns typical of real robotic operation.

The superior accuracy of our method is particularly evident in the window-building sequence, as shown in Fig. 14. While both CM-GAE and CMax-SLAM exhibit significant drift and inconsistent estimation across all three rotation angles, EROAM closely tracks the ground truth trajectory throughout the sequence. The detailed views between 15s and 20s clearly demonstrate our method’s ability to maintain accurate rotation estimation even during complex motion patterns.

This accuracy in rotation estimation directly translates to high-quality panoramic reconstruction results. As shown in Fig. 15, EROAM produces significantly clearer panoramas compared to CMax-SLAM. The comparison between the front-gate sequence results demonstrates our method’s superior performance in maintaining structural clarity and avoiding ghosting artifacts. This advantage is further emphasized in the embankment-360 sequence, where EROAM successfully reconstructs a complete  $360^\circ$  panorama with consistent quality.

Additional reconstruction results Fig. 16) demonstrate consistent performance across diverse environments.

### E. Runtime Analysis

Tab. VII and Tab. VIII present the runtime comparison of RTPT, CM-GAE, CMax-SLAM, and our EROAM method on both synthetic ECRot sequences and real-world EROAM-campus sequences. Note that SMT is excluded from the comparison as it fails to process any sequences successfully and exhibits prohibitively high computational costs even during failed attempts. All experiments were conducted on a laptop

with an Intel Core i9-14900HX CPU and 32GB RAM, with RTPT utilizing an NVIDIA RTX 4060 GPU while all other methods run on CPU only.

Our implementation uses a consistent processing frequency of  $f = 1000 \text{ Hz}$  across both datasets, demonstrating EROAM’s capability to handle different resolution inputs while maintaining real-time performance. Processing times may be slightly shorter than sequence durations, which is expected when measuring real-time processing performance.

EROAM demonstrates superior computational efficiency across both datasets. For synthetic data, our method processes most sequences in approximately 5s. On real-world data, taking the 31.413s embankment sequence as an example, EROAM achieves remarkable speedups:  $6.3\times$  compared to CM-GAE,  $5.3\times$  compared to RTPT (despite its GPU acceleration), and  $17.6\times$  compared to CMax-SLAM. CMax-SLAM’s performance degrades significantly with sequence duration due to its combination of contrast maximization and backend optimization, with processing time scaling poorly with event density. CM-GAE exhibits similar limitations. EROAM, in contrast, achieves real-time performance even for extended sequences - processing the 47.169s lawn sequence in 47.158s, while other methods require substantially longer: CM-GAE takes 1318.581s and CMax-SLAM needs 2553.260s.

This consistent performance stems from two key design choices. First, our spherical map representation significantly simplifies map maintenance. Unlike RTPT’s complex map updates and feature management operations, EROAM employs efficient incremental updates to its spherical map using an ikd-Tree and manages point density with Regional Density Management (RDM), substantially reducing computational overhead.

Second, our ES-ICP algorithm fundamentally avoids the computational bottlenecks inherent in contrast maximization-

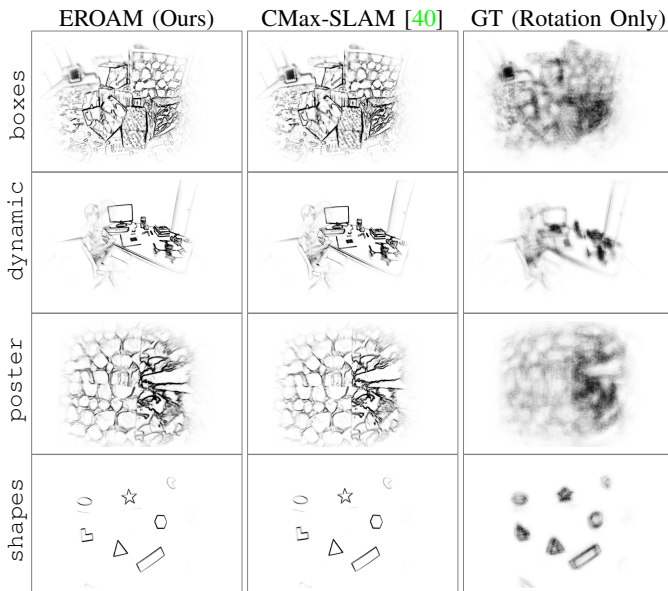


Fig. 17: Robustness evaluation on ECD dataset [60] with unmodeled translation. Left: EROAM. Middle: CMax-SLAM [40]. Right: GT rotation-only panorama. The severe blurring in GT panoramas confirms that parallax from translation makes quantitative rotation metrics misleading. Both methods produce coherent results despite minor translation, though edges are less sharp than in pure rotation scenarios.

TABLE IX: Quantitative evaluation on the ECD dataset [60].

Sequence	boxes		dynamic		poster		shapes	
	$\overline{ape}$ (°)	$\overline{rpe}$ (°)						
CMax-SLAM [40]	2.752	1.251	1.758	0.890	4.720	1.384	2.964	1.471
EROAM (ours)	2.680	1.138	2.491	0.918	4.711	1.310	3.135	1.404

based methods. While CM-GAE and CMax-SLAM require iterative contrast computation over event time windows and computationally intensive event warping operations after each velocity update, EROAM’s ES-ICP solution:

- Eliminates repeated event warping requirements
- Enables parallel processing of point-to-line distances and their Jacobians across CPU cores
- Maintains consistent computational load regardless of event rate or scene complexity

The experimental results clearly demonstrate EROAM’s superior computational efficiency and scalability. By maintaining real-time performance across both synthetic and real-world scenarios while requiring only CPU resources, EROAM presents a practical solution for event-based rotational motion estimation in real-world applications.

#### F. Robustness to Unmodeled Translational Motion

While EROAM is designed for pure rotational motion, some degree of translational motion is inevitable in practice. To evaluate robustness when this assumption is violated, we assess EROAM on the Event Camera Dataset (ECD) [60], which features unconstrained handheld 6-DOF motion with translation typically within  $\sim 0.3$  m and associated parallax effects, representing a more challenging scenario than our previous pure rotation evaluations. Following CMax-SLAM’s evaluation protocol [40], we process all four sequences (`boxes`,

`dynamic`, `poster`, and `shapes`), using the first 30 seconds of each.

Fig. 17 presents panoramic reconstructions from three sources. Critically, the rightmost column shows panoramas generated using only the rotational component of the 6-DOF ground truth. These are severely blurred and fail to register scene edges. This visualization confirms that when parallax from translation is present, even the ground truth rotation cannot properly align events, rendering it an invalid reference for performance evaluation.

In contrast, both EROAM (left column) and CMax-SLAM (middle column) produce coherent panoramic reconstructions, demonstrating that both methods can operate despite the presence of unmodeled translation. However, the reconstructed edges are noticeably less sharp compared to pure rotation scenarios (Fig. 9), which is expected since no single  $SO(3)$  trajectory can perfectly align all events when parallax exists.

For transparency and completeness, we report the quantitative  $\overline{ape}$  and  $\overline{rpe}$  metrics in Tab. IX. However, it is critical to emphasize that  $\overline{ape}$  and  $\overline{rpe}$  are not effective metrics for performance evaluation on these sequences. The ground truth motion is 6-DOF, yet this evaluation is constrained to only 3-DOF rotation. As Fig. 17 visually confirms with the severely blurred GT (Rotation Only) panorama, the 3-DOF rotational component of the ground truth is itself an invalid reference that fails to align the events due to significant translational parallax. Therefore, the quantitative results in this context cannot measure accuracy, their purpose is to demonstrate that EROAM and CMax-SLAM exhibit comparable behavior when processing this unmodeled translational motion, which aligns with our qualitative findings.

This experiment demonstrates EROAM’s robustness to moderate translational motion. However, when translation becomes substantially larger, the parallax effects overwhelm the pure rotation model, as discussed in Sec. V.

#### G. Ablation Studies

To analyze how different design choices and parameters affect EROAM’s performance, we present comprehensive ablation studies. These studies specifically investigate the impact of four key elements: the number of events per frame ( $n$ ), the processing frequency ( $f$ ), the ES-ICP distance metric (point-to-line vs. point-to-point), and the Regional Density Management (RDM) mechanism.

1) *Impact of Number of Events per Frame ( $n$ ):* The number of events  $n$  used per processing frame directly affects both the estimation accuracy and computational efficiency of our system. Tab. X presents results across various settings of  $n$ , evaluated on both synthetic ECRot and real-world EROAM-campus sequences.

The results indicate that a sufficient number of events is crucial for the ES-ICP algorithm to reliably establish geometric constraints and converge to an accurate solution. With very small event slices ( $n \leq 400$ ), ES-ICP struggles, leading to high error rates or complete tracking failures. For instance, with  $n = 200$ , all tested sequences show  $\overline{ape}$  exceeding  $110^\circ$ , indicating complete tracking loss. Performance stabilizes

TABLE X: Ablation study on the impact of  $n$ 

$n$	bicycle				town				distant-building				embankment			
	$\overline{ape}$ (°)	$\overline{rpe}$ (°)	$t_{es}$ (ms)	$t$ (s)	$\overline{ape}$ (°)	$\overline{rpe}$ (°)	$t_{es}$ (ms)	$t$ (s)	$\overline{ape}$ (°)	$\overline{rpe}$ (°)	$t_{es}$ (ms)	$t$ (s)	$\overline{ape}$ (°)	$\overline{rpe}$ (°)	$t_{es}$ (ms)	$t$ (s)
200	116.988	10.271	0.409	4.996	123.442	10.226	0.396	4.997	135.360	7.353	0.414	29.218	110.486	6.978	0.428	31.459
400	0.986	0.191	0.566	4.998	95.452	8.461	0.498	4.996	89.487	7.562	0.519	29.218	88.200	6.529	0.497	31.459
800	0.140	0.074	0.621	4.997	0.477	0.088	0.609	4.996	0.593	0.472	0.617	29.218	0.755	0.303	0.610	31.459
1600	0.121	0.038	0.693	5.003	0.234	0.053	0.718	4.997	0.231	0.234	0.625	29.218	0.558	0.236	0.692	31.459
3200	0.133	0.044	1.114	7.141	0.205	0.037	1.229	7.741	0.233	0.206	0.936	29.218	0.507	0.258	1.009	31.973
6400	0.124	0.039	1.339	8.442	0.162	0.041	2.183	13.647	0.246	0.224	1.405	34.069	0.528	0.280	1.603	45.870
12800	0.123	0.039	1.329	8.339	0.159	0.048	3.288	20.384	0.236	0.215	1.763	39.575	0.529	0.247	1.815	50.818

TABLE XI: Ablation study on the impact of frequency  $f$ 

$f$ (Hz)	bicycle				town				distant-building				embankment			
	$\overline{ape}$ (°)	$\overline{rpe}$ (°)	$t_{es}$ (ms)	$t$ (s)	$\overline{ape}$ (°)	$\overline{rpe}$ (°)	$t_{es}$ (ms)	$t$ (s)	$\overline{ape}$ (°)	$\overline{rpe}$ (°)	$t_{es}$ (ms)	$t$ (s)	$\overline{ape}$ (°)	$\overline{rpe}$ (°)	$t_{es}$ (ms)	$t$ (s)
50	94.866	52.260	1.630	4.966	100.675	34.735	1.551	4.954	138.721	11.231	1.603	29.189	11.963	4.581	1.405	31.449
100	18.819	0.608	2.141	4.977	65.508	3.022	1.869	4.974	0.258	0.196	1.731	29.199	0.693	0.272	1.744	31.449
200	1.001	0.076	1.922	4.983	19.086	0.580	1.683	4.978	0.248	0.251	1.398	29.204	0.490	0.292	1.617	31.449
400	0.071	0.042	1.301	4.983	2.376	0.131	1.240	4.992	0.224	0.194	1.200	29.207	0.444	0.216	1.230	31.449
800	0.091	0.045	0.831	4.986	0.193	0.063	0.823	4.979	0.255	0.276	0.810	29.208	0.439	0.295	0.800	31.450
1600	0.110	0.044	0.568	5.988	0.169	0.057	0.564	5.946	4.621	0.321	0.483	29.208	0.486	0.212	0.495	31.450
3200	0.206	0.050	0.419	8.920	0.205	0.066	0.539	11.281	7.973	0.325	0.422	32.730	0.481	0.266	0.469	43.780

significantly when  $n \geq 800$ , with  $\overline{ape}$  dropping to 0.140° for the `bicycle` sequence. For our main experiments, we selected  $n = 1500$ . This choice (approximated by  $n = 1600$  in the ablation table) effectively balances accuracy and computational load. At  $n = 1600$ , the ES-ICP computation time ( $t_{es}$ ) consistently remains between 0.62 ms and 0.72 ms, well within the 1 ms budget required for 1000 Hz operation. While further increasing  $n$  (to 3200, 6400, or 12800) might offer marginal accuracy improvements in some sequences, it significantly increases computation time. For instance,  $t_{es}$  exceeds 1 ms when  $n = 3200$ , reaching as high as 3.288 ms for the `town` sequence when  $n = 12800$ . Thus,  $n = 1500$  provides a practical trade-off, ensuring robust performance without compromising real-time capabilities.

2) *Effect of Processing Frequency ( $f$ ):* Processing frequency  $f$  determines how often rotation estimates are computed and directly impacts the system’s ability to track high-speed motions. Tab. XI shows performance across different frequency settings, with a fixed  $n = 1500$ .

High-frequency estimation is paramount for EROAM’s success. The Iterative Closest Point (ICP) algorithm, which ES-ICP is based on, is susceptible to converging to local minima if the initial guess for the transformation is not sufficiently close to the true solution. By operating at a high frequency (e.g., 1000 Hz), the actual rotation between consecutive frames becomes very small. When we use the solution from the previous ES-ICP step as the initial guess for the current frame, this initial guess is inherently very close to the true current pose. This dramatically improves the likelihood of ES-ICP converging to the correct global minimum, which is a core reason for EROAM’s high accuracy.

The experimental results support this understanding. At very low frequencies ( $f = 50$  Hz), large inter-frame rotations lead to significant tracking challenges, resulting in high errors or failures (e.g.,  $\overline{ape} = 94.866^\circ$  for `bicycle` at  $f = 50$  Hz). Performance improves substantially as frequency increases, with  $f \geq 400$  Hz providing consistently good results. At  $f = 800$  Hz, all sequences demonstrate excellent accuracy, with ES-ICP computation times ( $t_{es}$ ) under 0.9 ms.

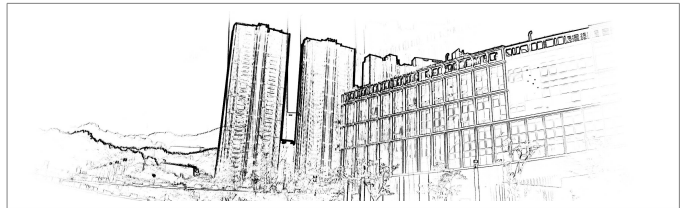


Fig. 18: Panoramic image generated using Point-to-Point (P2P) ES-ICP algorithm on the `distant-building` sequence. This result exhibits noticeable ghosting effects and misalignments compared to our proposed Point-to-Line (P2L) method shown in Fig. 16a. The P2P approach suffers from double edges and blurring, especially in building contours and architectural details.

Conversely, extremely high frequencies ( $f \geq 1600$  Hz), while maintaining good accuracy on some sequences, can lead to diminishing returns or even slight degradation. More importantly, they substantially increase total processing time due to the overhead of handling many more frames (e.g., processing time for `town` increases from 4.979 s at  $f = 800$  Hz to 11.281 s at  $f = 3200$  Hz).

Based on these findings, we selected  $f = 1000$  Hz as our standard operational frequency. This allows EROAM to process a relatively small number of events per frame but at an extremely high rate, offering an optimal balance between accuracy, robustness to dynamic motion, and computational efficiency.

3) *Point-to-Line vs. Point-to-Point ES-ICP:* To assess the impact of the ES-ICP distance metric, we compared our point-to-line (P2L) approach with a traditional point-to-point (P2P) implementation. The results are presented in Tab. XII, with a qualitative comparison shown in Fig. 18.

The P2L approach consistently outperforms P2P in terms of accuracy across all datasets. This advantage is crucial for robust tracking, as an erroneous estimate from P2P could negatively affect subsequent frames by providing a poor initial guess. The accuracy gap becomes particularly significant in challenging sequences. For example, on the

TABLE XII: Comparison between Point-to-Line (P2L) and Point-to-Point (P2P) methods

Dataset	P2L				P2P			
	$\overline{ape}$ (°)	$\overline{rpe}$ (°)	$t_{es}$ (ms)	$t$ (s)	$\overline{ape}$ (°)	$\overline{rpe}$ (°)	$t_{es}$ (ms)	$t$ (s)
bicycle	0.092	0.045	0.664	5.009	0.104	0.045	0.533	4.996
town	0.266	0.068	0.674	4.984	0.433	0.154	0.540	5.000
distant-building	0.274	0.249	0.605	29.209	1.938	1.138	0.488	29.218
embankment	0.439	0.252	0.689	31.449	0.947	0.270	0.509	31.459
DL-8	0.460	0.092	0.721	4.989	17.159	0.709	0.594	4.998
LT-80	0.140	0.063	0.683	80.122	0.175	0.082	0.476	80.001

TABLE XIII: Performance comparison with and without Regional Density Management (RDM)

Dataset	w/ RDM					w/o RDM				
	$\overline{ape}$ (°)	$\overline{rpe}$ (°)	$t_{es}$ (ms)	$t_{kd}$ (ms)	$t$ (s)	$\overline{ape}$ (°)	$\overline{rpe}$ (°)	$t_{es}$ (ms)	$t_{kd}$ (ms)	$t$ (s)
bicycle	0.119	0.041	0.635	234.223	4.996	0.137	0.038	0.691	409.045	5.014
town	0.177	0.035	0.639	221.014	4.995	0.206	0.037	0.685	410.574	5.006
distant-building	0.240	0.236	0.551	68.388	29.218	0.261	0.228	0.595	354.598	29.217
embankment	0.537	0.244	0.623	89.756	31.459	0.500	0.235	0.632	406.953	31.458
DL-8	0.226	0.066	0.692	632.552	4.998	0.284	0.061	2.151	2235.392	13.308
LT-80	0.140	0.069	0.665	1410.348	80.122	0.165	0.064	0.726	8930.521	80.770

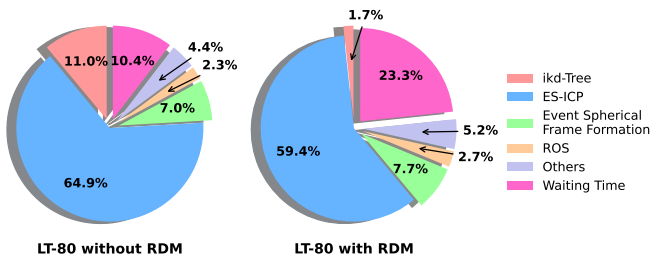


Fig. 19: Comparison of computational time distribution across EROAM components on the LT-80 sequence with and without Regional Density Management (RDM). The pie charts demonstrate how RDM optimizes processing efficiency by significantly reducing the ikd-Tree operation overhead.

distant-building sequence, P2L achieves an  $\overline{ape}$  of  $0.274^\circ$  compared to P2P’s  $1.938^\circ$ . The difference is even more dramatic for the dynamic DL-8 sequence, where P2L maintains accurate tracking ( $\overline{ape} = 0.460^\circ$ ) while P2P fails completely ( $\overline{ape} = 17.159^\circ$ ). As demonstrated by comparing our P2L result in Fig. 16a with the P2P result in Fig. 18, P2L’s superior accuracy translates to clearer panoramic reconstructions with well-aligned edges, whereas P2P results in noticeable ghosting and misalignments. This performance advantage stems from P2L’s ability to leverage local structural information by fitting lines to neighboring points rather than relying solely on individual point correspondences. By considering the underlying edge structure represented by multiple map points, P2L establishes more robust geometric constraints for alignment, especially in regions with sparse or uneven event distributions. While P2P offers computational advantages, with ES-ICP computation times approximately 20-30% faster than P2L due to simpler nearest neighbor operations and the elimination of line fitting, the substantial accuracy and robustness improvements provided by P2L, particularly in challenging scenarios, justify its selection as our standard approach. Furthermore, P2L itself remains computationally efficient. For applications where raw speed is paramount over accuracy in simpler scenes, our open-source implementation also includes the P2P option.

4) *Effectiveness of Regional Density Management:* Our Regional Density Management (RDM) approach is crucial for maintaining both long-term performance and map quality. Tab. XIII demonstrates its effectiveness by comparing EROAM’s performance with and without RDM, and Fig. 19 illustrates the impact on computational resource allocation.

The core challenge RDM addresses is map maintenance for real-time operation without sacrificing detail through spatial downsampling. As keyframes are continuously added to the

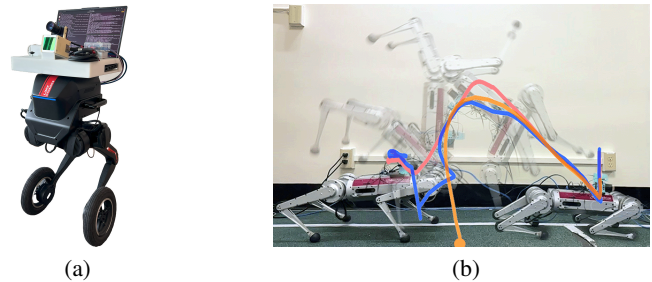


Fig. 20: Event camera-equipped robotic platforms. (a) The LimX TRON 1 wheeled bipedal robot, our experimental platform, equipped with an iniVation DVXplorer event camera. (b) A Mini-Cheetah quadruped robot with an event camera performing a backflip, featured in the CEAR dataset [64]. Image (b) from [65].

map (stored in an ikd-Tree), two issues arise: the time to update the ikd-Tree increases, and the growing number of points in the tree slows down nearest neighbor searches crucial for ES-ICP. This is especially problematic in long sequences or scenarios where the camera repeatedly scans the same area, leading to redundant points that bloat the map, degrade performance, and potentially reduce ES-ICP accuracy. RDM effectively mitigates these issues. While both approaches (with and without RDM) achieve comparable accuracy (similar  $\overline{ape}$  and  $\overline{rpe}$  values), RDM significantly improves computational efficiency. This is most evident in longer sequences like LT-80, where RDM reduces the k-d tree update time ( $t_{kd}$ ) by 84%, from 8930.521 ms to 1410.348 ms. Fig. 19 further clarifies RDM’s optimization of computational resources. Without RDM, ikd-Tree operations consume 11.0% of the total processing time. With RDM enabled, this overhead drops dramatically to just 1.7%. The ES-ICP time ( $t_{es}$ ) also sees a slight decrease with RDM, as a more efficiently managed map with fewer redundant points accelerates the nearest neighbor searches within ES-ICP. Notably, the Waiting Time (system idle time) increases from 10.4% to 23.3% with RDM, indicating that the system processes frames faster and has more performance headroom. These results validate our decision to incorporate RDM. It enables efficient map management by controlling point density without the accuracy loss associated with downsampling, ensuring detail preservation across all observed regions and robust real-time performance, especially during extended operation.

## V. LIMITATIONS

While EROAM demonstrates robustness to moderate translational motion as shown in IV-F, its performance degrades when translation becomes substantially larger. This limitation

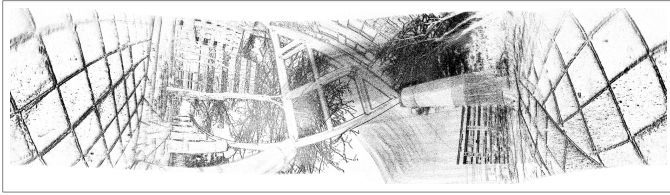


Fig. 21: Panoramic image reconstructed from the `env2_backflip1` sequence in [64]. The sequence was recorded with an event camera-equipped quadruped robot executing a backflip maneuver. The image is rotated  $90^\circ$ .

stems from the fundamental pure rotational motion assumption underlying our geometric formulation.

To illustrate this boundary, we evaluated EROAM on the `env2_backflip1` sequence from the CEAR dataset [64], which features a Mini-Cheetah quadruped robot [66] performing a backflip maneuver (Fig. 20b). This scenario combines three challenging factors: (1) large translation (0.7 m), (2) simultaneous  $360^\circ$  rotation, and (3) extreme close-range scenes (0.3–0.5 m) when facing the floor. Under these conditions, parallax effects become severe and the motion cannot be approximated as pure rotation.

Fig. 21 shows the panoramic reconstruction. While EROAM attempts to align events within its  $SO(3)$  framework, the estimated trajectory diverges from actual motion, incorrectly estimating completion of rotation before the backflip finishes. This causes misalignment manifesting as blurring and shadows in the panorama’s central region.

This failure case, combined with the successful ECD results (IV-F), empirically defines EROAM’s operational spectrum: the method maintains functionality with moderate translation (up to  $\sim 0.3$  m as in ECD sequences) but degrades when translation is substantially large and combined with close-range parallax. For applications requiring 6-DOF estimation in such scenarios, full SLAM systems would be more appropriate.

## VI. CONCLUSION

In this paper, we have introduced EROAM, a novel approach to event-based rotational motion estimation. Our method advances the state of the art through several key innovations. First, we propose a spherical representation that simplifies rotational motion formulation while operating in a continuous spherical domain. Second, we develop an Event Spherical ICP algorithm that efficiently processes events in parallel while maintaining high accuracy. Third, we present a real-time implementation that achieves superior performance. Through extensive evaluation on both synthetic and real-world datasets, we have demonstrated EROAM’s robust performance across various challenging conditions, including high angular velocities and extended sequences. The success of our ICP-based approach suggests promising potential for broader applications in event camera tasks, offering significant advantages in both computational efficiency and accuracy compared to existing contrast maximization frameworks.

## REFERENCES

- [1] D. Martinec and T. Pajdla, “Robust rotation and translation estimation in multiview reconstruction,” in *2007 IEEE conference on computer vision and pattern recognition*. IEEE, 2007, pp. 1–8.
- [2] P. Lichtsteiner, C. Posch, and T. Delbruck, “A  $128 \times 128$  120 db 15  $\mu$ s latency asynchronous temporal contrast vision sensor,” *IEEE journal of solid-state circuits*, vol. 43, no. 2, pp. 566–576, 2008.
- [3] C. Brandli, R. Berner, M. Yang, S.-C. Liu, and T. Delbruck, “A  $240 \times 180$  130 db 3  $\mu$ s latency global shutter spatiotemporal vision sensor,” *IEEE Journal of Solid-State Circuits*, vol. 49, no. 10, pp. 2333–2341, 2014.
- [4] G. Gallego, T. Delbrück, G. Orchard, C. Bartolozzi, B. Taba, A. Censi, S. Leutenegger, A. J. Davison, J. Conrath, K. Daniilidis *et al.*, “Event-based vision: A survey,” *IEEE transactions on pattern analysis and machine intelligence*, vol. 44, no. 1, pp. 154–180, 2020.
- [5] G. Gallego and D. Scaramuzza, “Accurate angular velocity estimation with an event camera,” *IEEE Robotics and Automation Letters*, vol. 2, no. 2, pp. 632–639, 2017.
- [6] J. Niu, S. Zhong, X. Lu, S. Shen, G. Gallego, and Y. Zhou, “Esvo2: Direct visual-inertial odometry with stereo event cameras,” *arXiv preprint arXiv:2410.09374*, 2024.
- [7] L. Gao, Y. Liang, J. Yang, S. Wu, C. Wang, J. Chen, and L. Kneip, “Vector: A versatile event-centric benchmark for multi-sensor slam,” *IEEE Robotics and Automation Letters*, vol. 7, no. 3, pp. 8217–8224, 2022.
- [8] W. Chamorro, J. Solà, and J. Andrade-Cetto, “Event-based line slam in real-time,” *IEEE Robotics and Automation Letters*, vol. 7, no. 3, pp. 8146–8153, 2022.
- [9] A. R. Vidal, H. Rebecq, T. Horstschaefer, and D. Scaramuzza, “Ultimate slam? combining events, images, and imu for robust visual slam in hdr and high-speed scenarios,” *IEEE Robotics and Automation Letters*, vol. 3, no. 2, pp. 994–1001, 2018.
- [10] S. Lin, Y. Zhang, D. Huang, B. Zhou, X. Luo, and J. Pan, “Fast event-based double integral for real-time robotics,” in *2023 IEEE International Conference on Robotics and Automation (ICRA)*. IEEE, 2023, pp. 796–803.
- [11] D. Qu, C. Yan, D. Wang, J. Yin, Q. Chen, D. Xu, Y. Zhang, B. Zhao, and X. Li, “Implicit event-rgbd neural slam,” in *Proceedings of the IEEE/CVF Conference on Computer Vision and Pattern Recognition*, 2024, pp. 19 584–19 594.
- [12] B. Kuang, E. Mueggler, G. Gallego, and D. Scaramuzza, “Low-latency visual odometry using event-based feature tracks,” in *2016 IEEE/RSSJ International Conference on Intelligent Robots and Systems (IROS)*. IEEE, 2016, pp. 16–23.
- [13] S. Sun, G. Cioffi, C. De Visser, and D. Scaramuzza, “Autonomous quadrotor flight despite rotor failure with onboard vision sensors: Frames vs. events,” *IEEE Robotics and Automation Letters*, vol. 6, no. 2, pp. 580–587, 2021.
- [14] D. Falanga, K. Kleber, and D. Scaramuzza, “Dynamic obstacle avoidance for quadrotors with event cameras,” *Science Robotics*, vol. 5, no. 40, p. eaaz9712, 2020.
- [15] C. Iaboni, H. Patel, D. Lobo, J.-W. Choi, and P. Abichandani, “Event camera based real-time detection and tracking of indoor ground robots,” *IEEE Access*, vol. 9, pp. 166 588–166 602, 2021.
- [16] A. Bhattacharya, M. Cannici, N. Rao, Y. Tao, V. Kumar, N. Matni, and D. Scaramuzza, “Monocular event-based vision for obstacle avoidance with a quadrotor,” *arXiv preprint arXiv:2411.03303*, 2024.
- [17] S. Afshar, N. Ralph, Y. Xu, J. Tapson, A. v. Schaik, and G. Cohen, “Event-based feature extraction using adaptive selection thresholds,” *Sensors*, vol. 20, no. 6, p. 1600, 2020.
- [18] H. Seok and J. Lim, “Robust feature tracking in dvs event stream using bézier mapping,” in *Proceedings of the IEEE/CVF Winter Conference on Applications of Computer Vision*, 2020, pp. 1658–1667.
- [19] Z. Huang, L. Sun, C. Zhao, S. Li, and S. Su, “Eventpoint: Self-supervised interest point detection and description for event-based camera,” in *Proceedings of the IEEE/CVF Winter Conference on Applications of Computer Vision*, 2023, pp. 5396–5405.
- [20] S. Lin, F. Xu, X. Wang, W. Yang, and L. Yu, “Efficient spatial-temporal normalization of sae representation for event camera,” *IEEE Robotics and Automation Letters*, vol. 5, no. 3, pp. 4265–4272, 2020.
- [21] A. Z. Zhu, N. Atanasov, and K. Daniilidis, “Event-based feature tracking with probabilistic data association,” in *2017 IEEE International Conference on Robotics and Automation (ICRA)*. IEEE, 2017, pp. 4465–4470.
- [22] S. Shiba, Y. Aoki, and G. Gallego, “Fast event-based optical flow estimation by triplet matching,” *IEEE Signal Processing Letters*, vol. 29, pp. 2712–2716, 2022.

- [23] M. Gehrig, M. Millhausler, D. Gehrig, and D. Scaramuzza, “E-raft: Dense optical flow from event cameras,” in *2021 International Conference on 3D Vision (3DV)*. IEEE, 2021, pp. 197–206.
- [24] S. Shiba, Y. Aoki, and G. Gallego, “Secrets of event-based optical flow,” in *European Conference on Computer Vision*. Springer, 2022, pp. 628–645.
- [25] C. Lee, A. K. Kosta, A. Z. Zhu, K. Chaney, K. Daniilidis, and K. Roy, “Spike-flownet: event-based optical flow estimation with energy-efficient hybrid neural networks,” in *European Conference on Computer Vision*. Springer, 2020, pp. 366–382.
- [26] C. Scheerlinck, H. Rebecq, D. Gehrig, N. Barnes, R. Mahony, and D. Scaramuzza, “Fast image reconstruction with an event camera,” in *Proceedings of the IEEE/CVF Winter Conference on Applications of Computer Vision*, 2020, pp. 156–163.
- [27] H. Rebecq, R. Ranftl, V. Koltun, and D. Scaramuzza, “Events-to-video: Bringing modern computer vision to event cameras,” in *Proceedings of the IEEE/CVF Conference on Computer Vision and Pattern Recognition*, 2019, pp. 3857–3866.
- [28] —, “High speed and high dynamic range video with an event camera,” *IEEE transactions on pattern analysis and machine intelligence*, vol. 43, no. 6, pp. 1964–1980, 2019.
- [29] S. Klenk, L. Koestler, D. Scaramuzza, and D. Cremers, “E-nerf: Neural radiance fields from a moving event camera,” *IEEE Robotics and Automation Letters*, vol. 8, no. 3, pp. 1587–1594, 2023.
- [30] I. Hwang, J. Kim, and Y. M. Kim, “Ev-nerf: Event based neural radiance field,” in *Proceedings of the IEEE/CVF Winter Conference on Applications of Computer Vision*, 2023, pp. 837–847.
- [31] V. Rudnev, M. Elgharib, C. Theobalt, and V. Golyanik, “Eventnerf: Neural radiance fields from a single colour event camera,” in *Proceedings of the IEEE/CVF Conference on Computer Vision and Pattern Recognition*, 2023, pp. 4992–5002.
- [32] Y. Xue, H. Li, S. Leutenegger, and J. Stuckler, “Event-based non-rigid reconstruction of low-rank parametrized deformations from contours,” *International Journal of Computer Vision*, pp. 1–19, 2024.
- [33] S. Lin, Y. Zhang, L. Yu, B. Zhou, X. Luo, and J. Pan, “Autofocus for event cameras,” in *Proceedings of the IEEE/CVF Conference on Computer Vision and Pattern Recognition*, 2022, pp. 16 344–16 353.
- [34] W. Liao, X. Zhang, L. Yu, S. Lin, W. Yang, and N. Qiao, “Synthetic aperture imaging with events and frames,” in *Proceedings of the IEEE/CVF Conference on Computer Vision and Pattern Recognition*, 2022, pp. 17 735–17 744.
- [35] B. He, Z. Wang, Y. Zhou, J. Chen, C. D. Singh, H. Li, Y. Gao, S. Shen, K. Wang, Y. Cao *et al.*, “Microsaccade-inspired event camera for robotics,” *Science Robotics*, vol. 9, no. 90, p. ead78124, 2024.
- [36] S. Lin, X. Zhang, L. Yang, L. Yu, B. Zhou, X. Luo, W. Wang, and J. Pan, “Neuromorphic synergy for video binarization,” *IEEE Transactions on Image Processing*, 2024.
- [37] T. Finateu, A. Niwa, D. Matolin, K. Tsuchimoto, A. Mascheroni, E. Reynaud, P. Mostafalu, F. Brady, L. Chotard, F. LeGoff *et al.*, “5.10 a 1280× 720 back-illuminated stacked temporal contrast event-based vision sensor with 4.86  $\mu\text{m}$  pixels, 1.066 geps readout, programmable event-rate controller and compressive data-formatting pipeline,” in *2020 IEEE International Solid-State Circuits Conference (ISSCC)*. IEEE, 2020, pp. 112–114.
- [38] H. Kim, A. Handa, R. Benosman, S.-H. Ieng, and A. J. Davison, “Simultaneous mosaicing and tracking with an event camera,” *J. Solid State Circ*, vol. 43, pp. 566–576, 2008.
- [39] C. Reinbacher, G. Munda, and T. Pock, “Real-time panoramic tracking for event cameras,” in *2017 IEEE International Conference on Computational Photography (ICCP)*. IEEE, 2017, pp. 1–9.
- [40] S. Guo and G. Gallego, “Cmax-slam: Event-based rotational-motion bundle adjustment and slam system using contrast maximization,” *IEEE Transactions on Robotics*, 2024.
- [41] H. Kim and H. J. Kim, “Real-time rotational motion estimation with contrast maximization over globally aligned events,” *IEEE Robotics and Automation Letters*, vol. 6, no. 3, pp. 6016–6023, 2021.
- [42] J. Zhang, S. Singh *et al.*, “Loam: Lidar odometry and mapping in real-time,” in *Robotics: Science and systems*, vol. 2, no. 9. Berkeley, CA, 2014, pp. 1–9.
- [43] T. Shan, B. Englot, D. Meyers, W. Wang, C. Ratti, and D. Rus, “Lio-sam: Tightly-coupled lidar inertial odometry via smoothing and mapping,” in *2020 IEEE/RSJ international conference on intelligent robots and systems (IROS)*. IEEE, 2020, pp. 5135–5142.
- [44] W. Xu and F. Zhang, “Fast-lío: A fast, robust lidar-inertial odometry package by tightly-coupled iterated kalman filter,” *IEEE Robotics and Automation Letters*, vol. 6, no. 2, pp. 3317–3324, 2021.
- [45] C. Bai, T. Xiao, Y. Chen, H. Wang, F. Zhang, and X. Gao, “Faster-lío: Lightweight tightly coupled lidar-inertial odometry using parallel sparse incremental voxels,” *IEEE Robotics and Automation Letters*, vol. 7, no. 2, pp. 4861–4868, 2022.
- [46] W. Xu, Y. Cai, D. He, J. Lin, and F. Zhang, “Fast-lío2: Fast direct lidar-inertial odometry,” *IEEE Transactions on Robotics*, vol. 38, no. 4, pp. 2053–2073, 2022.
- [47] S. Guo and T. Delbruck, “Low cost and latency event camera background activity denoising,” *IEEE Transactions on Pattern Analysis and Machine Intelligence*, vol. 45, no. 1, pp. 785–795, 2022.
- [48] D. Joubert, A. Marcireau, N. Ralph, A. Jolley, A. Van Schaik, and G. Cohen, “Event camera simulator improvements via characterized parameters,” *Frontiers in Neuroscience*, vol. 15, p. 702765, 2021.
- [49] L. Pan, C. Scheerlinck, X. Yu, R. Hartley, M. Liu, and Y. Dai, “Bringing a blurry frame alive at high frame-rate with an event camera,” in *Proceedings of the IEEE/CVF Conference on Computer Vision and Pattern Recognition*, 2019, pp. 6820–6829.
- [50] L. Pan, R. Hartley, C. Scheerlinck, M. Liu, X. Yu, and Y. Dai, “High frame rate video reconstruction based on an event camera,” *IEEE Transactions on Pattern Analysis and Machine Intelligence*, vol. 44, no. 5, pp. 2519–2533, 2020.
- [51] F. Paredes-Vallés and G. C. De Croon, “Back to event basics: Self-supervised learning of image reconstruction for event cameras via photometric constancy,” in *Proceedings of the IEEE/CVF Conference on Computer Vision and Pattern Recognition*, 2021, pp. 3446–3455.
- [52] G. Munda, C. Reinbacher, and T. Pock, “Real-time intensity-image reconstruction for event cameras using manifold regularisation,” *International Journal of Computer Vision*, vol. 126, no. 12, pp. 1381–1393, 2018.
- [53] G. Gallego, H. Rebecq, and D. Scaramuzza, “A unifying contrast maximization framework for event cameras, with applications to motion, depth, and optical flow estimation,” in *Proceedings of the IEEE conference on computer vision and pattern recognition*, 2018, pp. 3867–3876.
- [54] S. Shiba, Y. Aoki, and G. Gallego, “Event collapse in contrast maximization frameworks,” *Sensors*, vol. 22, no. 14, p. 5190, 2022.
- [55] Z. Zhang, “A flexible new technique for camera calibration,” *IEEE Transactions on pattern analysis and machine intelligence*, vol. 22, no. 11, pp. 1330–1334, 2000.
- [56] Y. Cai, W. Xu, and F. Zhang, “ikd-tree: An incremental kd tree for robotic applications,” *arXiv preprint arXiv:2102.10808*, 2021.
- [57] J. Sturm, N. Engelhard, F. Endres, W. Burgard, and D. Cremers, “A benchmark for the evaluation of rgb-d slam systems,” in *2012 IEEE/RSJ international conference on intelligent robots and systems*. IEEE, 2012, pp. 573–580.
- [58] M. Grupp, “evo: Python package for the evaluation of odometry and slam.” <https://github.com/MichaelGrupp/evo>, 2017.
- [59] H. Rebecq, D. Gehrig, and D. Scaramuzza, “Esim: an open event camera simulator,” in *Conference on robot learning*. PMLR, 2018, pp. 969–982.
- [60] E. Mueggler, H. Rebecq, G. Gallego, T. Delbruck, and D. Scaramuzza, “The event-camera dataset and simulator: Event-based data for pose estimation, visual odometry, and slam,” *The International Journal of Robotics Research*, vol. 36, no. 2, pp. 142–149, 2017.
- [61] W. Xing, S. Lin, L. Yang, and J. Pan, “Target-free extrinsic calibration of event-lidar dyad using edge correspondences,” *IEEE Robotics and Automation Letters*, vol. 8, no. 7, pp. 4020–4027, 2023.
- [62] D. He, W. Xu, N. Chen, F. Kong, C. Yuan, and F. Zhang, “Point-lío: Robust high-bandwidth light detection and ranging inertial odometry,” *Advanced Intelligent Systems*, vol. 5, no. 7, p. 2200459, 2023.
- [63] C. Yuan, X. Liu, X. Hong, and F. Zhang, “Pixel-level extrinsic self calibration of high resolution lidar and camera in targetless environments,” *IEEE Robotics and Automation Letters*, vol. 6, no. 4, pp. 7517–7524, 2021.
- [64] S. Zhu, Z. Xiong, and D. Kim, “Cear: Comprehensive event camera dataset for rapid perception of agile quadruped robots,” *IEEE Robotics and Automation Letters*, 2024.
- [65] S. Zhu, Z. Tang, M. Yang, E. Learned-Miller, and D. Kim, “Event camera-based visual odometry for dynamic motion tracking of a legged robot using adaptive time surface,” in *2023 IEEE/RSJ International Conference on Intelligent Robots and Systems (IROS)*. IEEE, 2023, pp. 3475–3482.
- [66] B. Katz, J. Di Carlo, and S. Kim, “Mini cheetah: A platform for pushing the limits of dynamic quadruped control,” in *2019 international conference on robotics and automation (ICRA)*. IEEE, 2019, pp. 6295–6301.